

Manuscript Number: APCATA-D-19-00233R2

Title: $Cu_xCeMgAlO$ mixed oxide catalysts derived from multicationic LDH precursors for methane total oxidation

Article Type: Research Paper

Keywords: layered double hydroxides; mixed oxides catalysts; copper; cerium; methane combustion.

Corresponding Author: Dr. Ioan-Cezar Marcu, Ph. D.

Corresponding Author's Institution: University of Bucharest

First Author: Hussein Mahdi S Al-Aani, PhD student

Order of Authors: Hussein Mahdi S Al-Aani, PhD student; Emmanuel Iro, PhD; Pramodh Chirra; Ioana Fechete, PhD; Mihaela Badea, PhD; Catalin Negrila, PhD; Ionel Popescu, PhD; Maria Olea, Prof.; Ioan-Cezar Marcu, Ph. D.

Abstract: Five $Cu(x)CeMgAlO$ mixed oxides with different copper contents (x) ranging from 6 to 18 at. % with respect to cations, but with fixed 10 at. % Ce and Mg/Al atomic ratio of 3, were prepared by thermal decomposition of LDH precursors at 750 °C. $Cu(15)CeMgAlO$ was also calcined at 550 and 650 °C. They were characterized by XRD, SEM-EDX, nitrogen adsorption/desorption, H_2 -TPR, XPS and DR-UV-Vis techniques. Their catalytic properties in the total oxidation of methane were evaluated and compared with those of an industrial Pd/Al₂O₃ catalyst. $Cu(15)CeMgAlO$ was the most active catalyst in this series, with a T50 value of only ca. 45 °C higher than that of Pd/Al₂O₃. This difference becomes as low as ca. 25 °C for the $Cu(15)CeMgAlO$ system calcined at 550 °C. The excellent stability on stream of the $Cu(15)CeMgAlO$ catalyst was evidenced.



UNIVERSITY OF BUCHAREST
FACULTY OF CHEMISTRY
Laboratory of Chemical Technology & Catalysis
4-12, Blv. Regina Elisabeta, 030018 Bucharest ROMANIA
Fax + 40213159249; Tel. + 40213051464
ioancezar.marcu@chimie.unibuc.ro
unibuc.ro/user/ioan.cezar.marcu/

Dr. Habil. Ioan-Cezar Marcu
Associate Professor

Bucharest, August 9, 2019

Attn: *Prof. Jose M. Lopez Nieto*, Editor
Applied Catalysis A: General

Dear Editor,


Please find our revised paper entitled “Cu_xCeMgAlO mixed oxide catalysts derived from multicationic LDH precursors for methane total oxidation”, authors Hussein Mahdi S. AL-AANI, Emmanuel IRO, Pramodh CHIRRA, Ioana FECHETE, Mihaela BADEA, Cătălin NEGRILĂ, Ionel POPESCU, Maria OLEA and Ioan-Cezar MARCU, which we would like to publish in *Applied Catalysis A: General*.

We addressed all the issues raised by the Reviewer #2 and provided a point by point response to them.

The submission is original, not under consideration for publication elsewhere. All the authors are aware of the submission of the revised version and agree to its publication in *Applied Catalysis A: General*.

Thank you for reconsidering our revised manuscript.

With best regards,


Ioan-Cezar Marcu

Reviewer #1: I suggest the acceptance of the manuscript in the present form.

Thank you!

Reviewer #2: After the revisions, this paper could be accepted for a publication after some major revisions.

1: The Table 2 and Table 3 were suggested to be improved.

Answer: Tables 2 and 3 show the bulk composition of both precursors and mixed oxides determined by EDX and the surface composition of the mixed oxides catalysts determined by XPS, respectively. Firstly, because the precursors are not pure LDH phases, on the one hand, and the mixed oxides adsorb variable amounts of water and carbon dioxide from the environment, on the other hand, relevant for the composition of these materials is the cationic content. Therefore, Table 2 shows the cationic content (at. %) as determined by EDX analysis (the average of four different points) together with relevant cationic ratios. Secondly, Table 3 shows the surface cationic composition together with surface oxygen and carbon contents of the mixed oxide catalysts which are relevant for the discussion. However, to easily compare the bulk and surface cationic compositions, relevant surface cationic ratios were presented in Table 3. All these composition data have been discussed in the manuscript. Tables 2 and 3 have not been changed.

2: The CH₄ was one of the Greenhouse gas (CH₄ effect was much higher than that of CO₂), whether 100% conversion of methane could be achieved?

Please give some experimental data, or some analysis based on the literature works.

Answer: We added in Section 3.2 the following sentences (yellow-highlighted in the revised manuscript):

“The complete conversion of methane was achieved at 600 °C (T₁₀₀) for both Cu(15)CeMgAlO and Cu(18)CeMgAlO systems, temperature which is only 30 °C higher than that corresponding to the Pd/Al₂O₃ catalyst.”

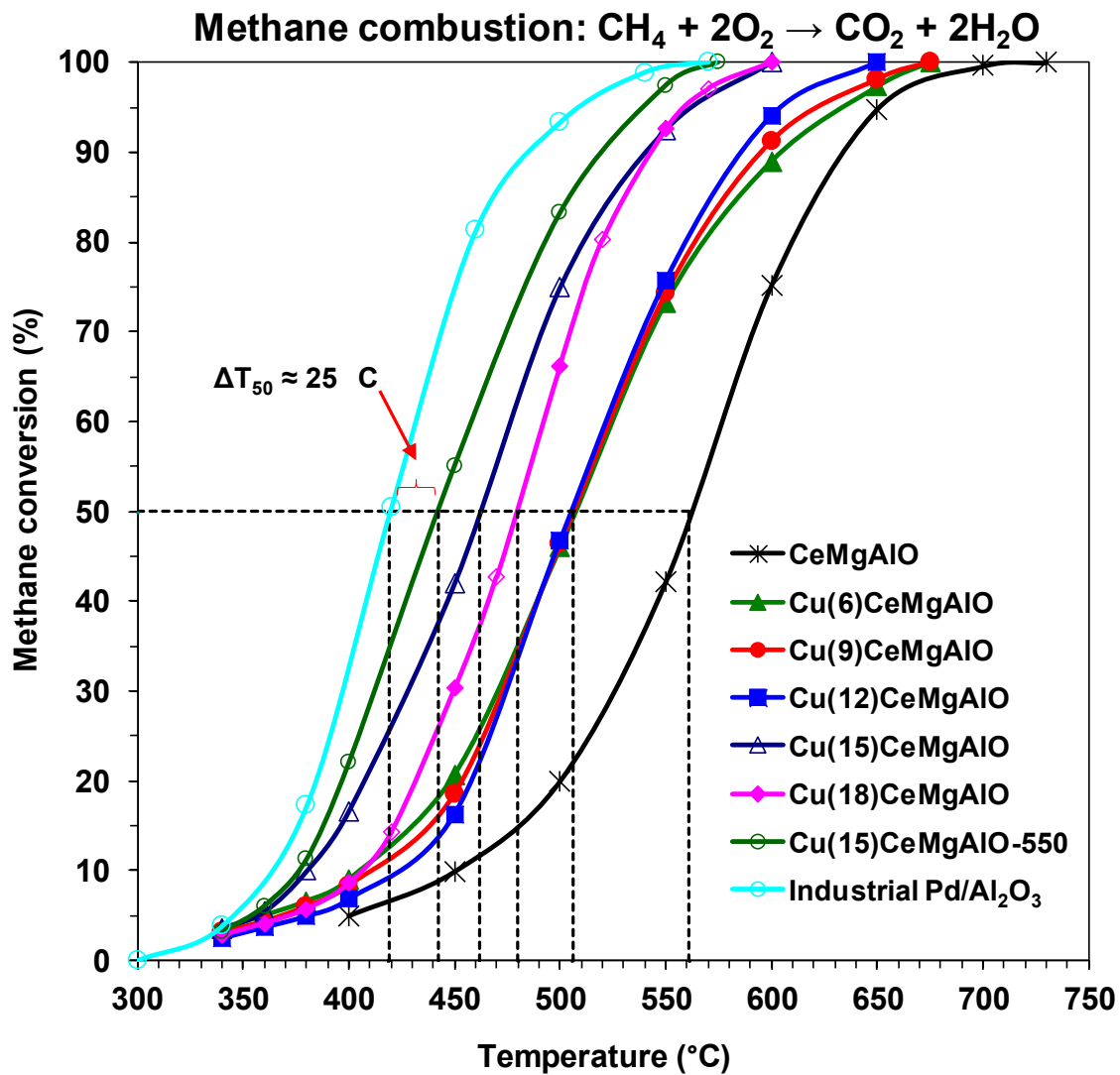
“It is worth noting that the T₅₀ and T₁₀₀ values for the Cu(15)CeMgAlO-550 catalyst are only ca. 25 and 5 °C, respectively, higher than those of the commercial Pd/Al₂O₃ catalyst.”

3: There were data of apparent activation Energy for the samples, some related comparison analysis or discussions were preferred.

Answer: The apparent activation energy values reported in Table 5 were in detail discussed and compared (with literature as well) in Section 3.2 (see the green-highlighted text in the revised manuscript, please).

Al-Aani et al.

Graphical abstract



Al-Aani et al.

Research highlights

- > Complex Cu(x)CeMgAl mixed oxides have been synthesized from LDH-based precursors.
- > Cu(15)CeMgAlO is the most active and highly stable catalyst.
- > T₅₀ value is only ca. 25 °C higher than that of an industrial Pd/Al₂O₃ catalyst.
- > Cu dispersion and Cu-Ce interaction determine the catalytic activity.
- > Increasing calcination temperature strengthens the Cu-Ce interaction.

Cu_xCeMgAlO mixed oxide catalysts derived from multicationic LDH precursors for methane total oxidation

Hussein Mahdi S. AL-AANI¹, Emmanuel IRO², Pramodh CHIRRA², Ioana FECHETE³, Mihaela BADEA⁴, Cătălin NEGRILĂ⁵, Ionel POPESCU⁶, Maria OLEA², Ioan-Cezar MARCU^{*, 1, 6}

¹ Laboratory of Chemical Technology and Catalysis, Department of Organic Chemistry, Biochemistry and Catalysis, Faculty of Chemistry, University of Bucharest, 4-12, Blv. Regina Elisabeta, 030018, Bucharest, Romania

² School of Science, Engineering & Design, Teesside University, Middlesbrough TS1 3BX, United Kingdom

³ International Center for CVD Innovation-Nogent, Pole Technologique Sud Champagne, Université de Troyes-Antenne de Nogent, 26, rue Lavoisier, 52800 Nogent, France

⁴ Department of Inorganic Chemistry, Faculty of Chemistry, University of Bucharest, 90-92 Panduri Str., 050663, Bucharest, Romania

⁵ National Institute of Material Physics, P. O. Box MG 7, Măgurele, Romania

⁶ Research Center for Catalysts and Catalytic Processes, Faculty of Chemistry, University of Bucharest, 4-12 Blv Regina Elisabeta, 030018, Bucharest, Romania

Abstract

A series of five Cu(x)CeMgAlO mixed oxides with different copper contents (x) ranging from 6 to 18 at. % with respect to cations, but with fixed 10 at. % Ce and Mg/Al atomic ratio of 3, were prepared by thermal decomposition of layered double hydroxide (LDH) precursors at 750 °C. The solid containing 15 at. % Cu, i.e. Cu(15)CeMgAlO, was also calcined at 550 and 650 °C. Powder XRD was used to characterize the crystalline structure and SEM-EDX was used to monitor the morphology and chemical composition of both as prepared and calcined materials.

* Corresponding author. Phone: +40213051464; Fax: +40213159249; E-mail addresses: ioancezar.marcu@chimie.unibuc.ro , ioancezar_marcu@yahoo.com

Additionally, the textural properties and the reducibility of the mixed oxide catalysts were studied by nitrogen adsorption/desorption and temperature programmed reduction with hydrogen (H_2 -TPR) techniques, respectively. X-ray photoelectron spectroscopy (XPS) was used to determine the chemical state of the elements on the catalyst surface and the diffuse reflectance UV-Vis spectroscopy, to obtain information about the stereochemistry and aggregation of copper in the Cu-containing mixed oxides. Their catalytic properties in the total oxidation of methane, used as a volatile organic compound (VOC) model molecule, were evaluated and compared with those of an industrial Pd/Al₂O₃ catalyst. Their catalytic behavior was explained in correlation with their physicochemical properties. Cu(15)CeMgAlO mixed oxide was shown to be the most active catalyst in this series, with a T₅₀ (temperature corresponding to 50 % methane conversion) value of only ca. 45 °C higher than that of a commercial Pd/Al₂O₃ catalyst. This difference becomes as low as ca. 25 °C for the Cu(15)CeMgAlO system calcined at 550 °C. The influences of the contact time and of the methane concentration in the feed gas on the catalytic performances of the Cu(15)CeMgAlO catalyst have been investigated and its good stability on stream was evidenced.

Keywords: layered double hydroxides, mixed oxides catalysts, copper, cerium, methane combustion

1. Introduction

Volatile organic compounds (VOC), resulting from various industrial processes, but also from transportation and other activities, represent an important class of air pollutants [1]. Besides the direct harmful effects on human health, these compounds also contribute to the increasing of photochemical smog, formation of ground-level ozone and atmospheric ozone destruction [2-4]. Methane is a major hydrocarbon air pollutant of particular importance in global climate change, occupying the second place after carbon dioxide among the anthropogenic greenhouse gases (GHG) emitted at the global scale [5]. The Global Warming Potential (GWP) is used to compare the ability of GHG to trap heat and their persistence in the atmosphere, and methane has a GWP 25 times higher than CO₂ over a 100-year time horizon [6]. On the other hand, being the most

difficult organic molecule to oxidize due to its high stability, methane is often used as a test molecule in catalytic combustion of VOC [7].

VOC recovery from the residual gaseous effluents from different industrial processes is economically disadvantageous due to their very low concentrations and, therefore, their destruction is the only viable alternative [1, 8]. One of the main processes for the destruction of VOC is the catalytic combustion, which have some important advantages compared to traditional flame combustion [9, 10]. Thus, this process uses lower temperatures for the complete oxidation, which leads to lower energy consumption and also to the control of NO_x formation, avoiding, at the same time, the appearance of incomplete oxidation products [11-13].

The most active catalysts for VOC destruction belong to two main categories: supported noble metals and transition metal oxides [14, 15]. The supported noble metals, like Pd or Pt, are the most active catalysts for this process, which is their main advantage compared to the oxide-based catalysts [1, 16, 17]. Nevertheless, the noble metal-based catalysts have some major disadvantages: they are expensive and, because of their volatility and high sintering rates, they are easily deactivated at elevated temperatures [18]. Additionally, they may be deactivated by poisoning under the operating conditions [19]. Therefore, much effort has been made in the last years toward the design of new single and mixed transition-metal oxides catalysts to replace the noble metals for VOC abatement, a high number of research papers being published on this subject, which engendered several review papers and book chapters focusing either on catalytic combustion of VOC [20-23] and methane [24], or on different types of oxide catalysts, such as cobalt oxides [25], mesoporous silica-supported catalysts [26], ordered porous transition metal oxides [27], pillared clays [28, 29] and layered double hydroxide-derived mixed oxides [30].

Among the transition-metal mixed oxides, those obtained from layered double hydroxides (LDH) precursors were proven to have great potential as combustion catalysts, as they have high specific surface areas, high thermal stability and tunable redox and acid-base properties [30]. Indeed, it has been shown that mesoporous MMgAlO mixed oxide catalysts (M = Mn, Fe, Co, Ni, Cu, Zn, Ag and Pd), obtained by thermal decomposition of LDH precursors, are promising catalysts for the total oxidation of short-chain hydrocarbons [31]. Among the non-noble metal-containing catalysts, the Cu-containing system has been shown to be the most active in methane combustion, being also highly stable in the reaction conditions. Its catalytic activity depends on

the Cu content, the optimum being of ca. 12 at. % Cu and corresponds to the best dispersion of the copper-containing species in the MgAlO matrix [32]. On the other hand, from a series of lanthanide-containing LDH-derived mixed oxides catalysts, LnMgAlO (Ln = Ce, Sm, Dy and Yb), the Ce-containing one turned out to be the most active in methane combustion, the optimum content being ca. 10 at. % Ce [33]. Therefore, in an attempt to converge the benefits of preparation of mixed oxides from LDH precursors with the high activity of Cu-based systems in methane combustion and taking into consideration an expected Cu-Ce synergistic effect [34, 35], the present work investigates a series of new LDH-derived Cu-Ce-MgAl mixed oxides with 10 at. % Ce and different Cu content ranging from 6 to 18 at. %.

2. Experimental section

2.1. Catalysts preparation

A series of five Cu(x)CeMgAl LDH precursors with different copper contents ranging from 6 to 18 at. % with respect to cations, but with fixed 10 at. % Ce and Mg/Al atomic ratio of 3, were prepared by coprecipitation under ambient atmosphere. In a typical procedure, a mixed salts solution (200 mL) of Mg(NO₃)₂·6H₂O, Al(NO₃)₃·9H₂O and Cu(NO₃)₂·3H₂O and an alkaline solution of NaOH (2 M) were simultaneously added dropwise into a beaker containing 200 mL of cerium nitrate solution (Ce(NO₃)₃·6H₂O) at room temperature with controlled rate to maintain the pH close to 10. After complete precipitation, the slurry was aged at 80 °C overnight under vigorous stirring. The suspension was then separated by centrifugation, washed with deionized water and finally dried overnight at 80 °C. The Cu(x)CeMgAlO catalysts (with x = 6, 9, 12, 15 and 18 at. %, respectively) were obtained by calcination of their corresponding LDH precursors in air at 750 °C for 8 h. The Cu-free CeMgAl LDH precursor and the corresponding CeMgAlO mixed oxide were obtained following the same protocol.

In order to investigate the influence of the calcination temperature on the catalytic properties of the mixed oxides, the Cu(15)CeMgAl LDH precursor was also calcined at 550 and 650 °C, the resulting mixed oxides being noted Cu(15)CeMgAlO-550 and Cu(15)CeMgAlO-650, respectively.

2.2. Catalysts characterization

Powder X-ray diffraction (XRD) patterns of both precursors and mixed oxides were recorded on a Siemens D500 powder X-ray diffractometer with Bragg-Brentano geometry using nickel-filtered Cu-K α radiation ($\lambda = 0.15406$ nm). They were recorded over the 5-70° 2 θ angular range at a scanning rate of 1° min⁻¹. Crystalline phases were identified using standard JCPDS files.

Scanning electron microscopy (SEM) together with X-ray energy dispersion analysis (EDX) were used to monitor the morphology and chemical composition of both precursors and mixed oxides. SEM/EDX examination was performed using a Hitachi S-3400N microscope operated at an accelerating voltage of 20 kV. Four different points were analyzed on each sample.

X-ray photoelectron spectroscopy (XPS) was employed to determine the chemical state of the elements on the catalyst surface with a SPECS spectrometer equipped with a PHOIBOS 150 analyzer using a monochromatic Al K α radiation source (1486.7 eV). The acquisition was operated at a pass energy of 20 eV for the individual spectral lines and 50 eV for the extended spectra. The analysis of the spectra has been performed with the Spectral Data Processor v2.3 software using Voigt functions and usual sensitivity factors.

The textural characterization was performed using the conventional nitrogen adsorption/desorption method, with a Micromeritics ASAP 2010 automatic equipment. The surface areas were calculated using the BET method in the relative pressure, P/P_0 , region 0.065-0.2, while the pore sizes were determined by the BJH method from the nitrogen desorption branch. Prior to nitrogen adsorption, the oxide samples were degassed at 300 °C for 12 h.

The reducibility of the catalysts was studied by temperature programmed reduction under hydrogen (H₂-TPR). Experiments were performed using a CATLAB microreactor – MS system (Hiden Analytical, UK) under a flow of 5 % H₂ in Ar mixture (flowrate 30 mL min⁻¹) through the CATLAB's packed micro-reactor (4 mm internal diameter and length 18.5 cm) containing about 35 mg of sample, which was heated at a constant rate of 10 °C min⁻¹ up to 800 °C. The system was maintained for 1 h at 800 °C under H₂/Ar flow to complete the reduction.

Diffuse reflectance UV-Vis spectra were recorded in the range 200-1300 nm, using Spectralon as a standard, in a Jasco V 670 spectrophotometer. The obtained reflectance spectra were converted into the dependencies of Kubelka-Munk function on the absorption energy.

2.3. Catalytic test

The catalytic tests for the methane combustion over the mixed oxide catalysts were carried out in a fixed bed quartz tube down-flow reactor at atmospheric pressure. If not otherwise specified, a mixture of CH₄ and air containing 1 vol. % methane was passed through 1 cm³ (ca. 0.9 g) catalyst bed with a total flow rate of 267 mL min⁻¹ corresponding to a gas hourly space velocity (GHSV) of 16000 h⁻¹. For comparison, an industrially used Pd/Al₂O₃ catalyst (supplied by ARPECHIM Pitești, Romania) was tested in methane combustion in similar conditions, with a GHSV of 20000 h⁻¹. Before testing, the catalyst was pre-treated for 30 min in a stream of nitrogen at 600 °C (500°C for the sample calcined at 550 °C) for cleaning its surface. After pre-treatment, the catalyst was cooled down to 300 °C and the reaction was started by introducing the reaction mixture. Activity measurements were performed by increasing the reaction temperature from 300 to 650 °C at regular intervals. The reactants and product gases were analyzed on-line by a Clarus 500 Gas-Chromatograph equipped with a thermal conductivity detector, using two packed columns in series (6 ft Hayesep and 10 ft molecular sieve 5 Å). The catalysts activity was characterized by T₁₀, T₅₀ and T₉₀ representing the temperatures of methane conversions of 10, 50 and 90 %, respectively. The conversion was calculated as the amount of methane transformed in the reaction divided by the amount that was fed to the reactor by using the following formula:

$$\text{Conversion (\%)} = \frac{C_{CH_4,in} - C_{CH_4,out}}{C_{CH_4,in}} \times 100$$

where $C_{CH_4,in}$ and $C_{CH_4,out}$ represent the methane concentration (v/v) in the feed and effluent gases, respectively.

Complete selectivity to CO₂ and H₂O was always observed. The carbon balance was calculated based on the following equation:

$$C_{CH_4,in} = C_{CH_4,out} + C_{CO_2,out}$$

where $C_{CO_2,out}$ is the concentration of carbon dioxide (v/v) in the effluent gas. It was satisfactory in all runs to within ± 2 %.

3. Results and discussion

3.1. Catalysts characterization

The XRD patterns of the as-prepared precursor samples are displayed in Fig. 1. It can be observed that all the precursors consist of poorly crystallized LDH (JCPDS 37-0630) and boehmite AlOOH (JCPDS 83-2384) phases. The absence of diffraction lines corresponding to copper- or cerium-containing additional phases can be noted suggesting that these cations are well dispersed in the precursor samples.

For all the Cu(x)CeMgAlO catalysts, Mg(Al)O mixed oxide phase with the periclase-like structure (JCPDS-ICDD4-0829) and CeO₂ fluorite phase (JCPDS 75-0076) were identified (Fig. 2a). Except for Cu(18)CeMgAlO system, no diffraction lines corresponding to CuO phase were observed suggesting that copper is well dispersed in the Cu(x)CeMgAlO catalysts with x < 18.

Unexpectedly, the value of the lattice parameter, *d*, of the fluorite structure of the ceria phase calculated using the Bragg's law, from the three most intense lines in the diffractograms, i.e. (111), (220) and (311), increases with increasing Cu content in the Cu(x)CeMgAlO catalysts (Table 1). Indeed, taking into consideration that the radius of Cu²⁺ ion is lower than that of Ce⁴⁺, and those of Cu⁺ and Ce⁴⁺ ions are similar, the lattice parameter should decrease with increasing Cu content [36, 37]. Compared to the theoretical value of the ceria lattice parameter of 0.5411 nm [38], that of the samples with x < 12 is lower, and that of the samples with x ≥ 12 is even higher. This suggests the incorporation of copper into the ceria lattice at low Cu content, while at high Cu content ceria crystallites coexist with separate CuO particles, the latter being well developed in the Cu(18)CeMgAlO mixed oxide, in line with its XRD pattern. This is in agreement with the observed decrease of Cu solubility in ceria with increasing the grain size of the latter, resulting in the segregation of copper to the grain boundaries [39].

The full-width at half-maximum (FWHM) of the three most intense reflections of CeO₂ phase allows estimating the average crystallite size using the Debye-Scherrer equation:

$$D \approx \frac{1.08\lambda}{(2\theta)_{FWHM} \cos \theta}$$

where *D* is the crystallite size, *λ* is the wavelength of the Cu K-alpha radiation (0.15406 nm), *θ* is the Bragg diffraction angle. They are presented in Table 1. It can be observed that the crystallite size of ceria continuously increases with increasing the Cu content in the catalyst from 6.3 nm for Cu(6)CeMgAlO to 15.1 nm for Cu(18)CeMgAlO. A similar behavior has already been observed for coprecipitated CuO-CeO₂ mixed oxides [40].

Taking into consideration that the Ce content is almost constant in all the mixed oxide samples, it can be concluded that at low Cu content highly dispersed Cu-doped ceria crystallites are formed in the Mg(Al)O matrix, while at high Cu content larger ceria crystallites coexist with CuO particles that form a separate phase identified by XRD in the Cu(18)CeMgAlO mixed oxide. This reflects the low solubility of Cu ions in ceria [41].

The effect of calcination temperature on the XRD pattern of the Cu(15)CeMgAlO mixed oxide is shown on Fig. 2b. It can be observed that the diffraction lines of both Mg(Al)O mixed oxide and CeO₂ fluorite phases become significantly larger when the calcination temperature decreases from 750 to 650 °C suggesting a strong decrease of the crystallite size. Indeed, the average crystallite size of ceria decreases from 12.2 nm for the sample calcined at 750 °C to 4.1 nm for that calcined at 650 °C (Table 1). Further decreasing the calcination temperature from 650 to 550 °C results in slightly larger and less intense diffraction lines accounting for a lower crystallinity of the sample Cu(15)CeMgAlO-550. The average crystallite size of ceria slightly decreases from 4.1 nm for Cu(15)CeMgAlO-650 to 3.1 nm for Cu(15)CeMgAlO-550 (Table 1).

It is worth noting that the XRD patterns of the catalysts remain unchanged after the catalytic tests as it can be observed in Fig. S1 for the Cu(x)CeMgAlO samples with $x = 6, 12$ and 18 , respectively.

The cationic composition of both LDH precursors and calcined oxide catalysts has been determined by EDX spectroscopy and it is tabulated in Table 2. It can be observed that in both as-prepared and calcined samples the cationic content is close to the theoretical values within the limits of experimental error of the method used. The Mg/Al atomic ratio was very close to the fixed value of 3, while the Cu/Ce atomic ratio was slightly higher than the fixed value.

The SEM micrographs of both as-prepared and calcined Cu(x)CeMgAl samples are shown in Fig. S2. It can be observed that there are no significant differences between the particle morphologies of the precursors, on one hand, and of the calcined oxides, on the other hand. More unexpected, no significant differences can be observed between the particle morphologies of the precursors and of the corresponding mixed oxides. This indicates that neither the Cu content within the range 6-18 at. %, nor the calcination temperature up to 750 °C influence the particle morphology of the studied materials.

X-ray photoelectron spectroscopy (XPS) has been used to investigate the oxidation states of the different elements and the surface composition of the Cu(x)CeMgAlO mixed oxides. All the expected elements, i.e. Cu, Ce, Mg, Al, O and C are present on their surface (Table 3). The O 1s core level XPS spectra (Fig. 3a) showed for all the samples a peak deconvoluted into two components which could be related to lattice oxygen in oxide (BE ca. 529.7 eV) and oxygen in the lateral structure (BE ca. 531.6 eV), respectively [42]. The oxygen in the lateral structure corresponds to hydroxyl and/or carbonate species [43] and also to subsurface oxygen ions with particular coordination and lower electron density than the lattice oxygen [42]. The component at 531.6 eV obviously accounts for the hydroxylation and carbonation of the catalyst surface, as its relative intensity increased linearly with the specific surface area of the catalyst (Fig. S3), except for Cu(18)CeMgAlO sample. For the latter, the subsurface oxygen ions with particular coordination, probably located at the interface of the crystalline CuO and CeO₂ phases, also have an important contribution to the XPS peak at 531.6 eV. The C 1s core level (Fig. 3b) shows two main contributions: the adventitious hydrocarbon species (BE 284.8 eV) and carbon in carbonate (BE ca. 289.2 eV) [43]. These results confirm the need of pretreating the catalysts in the reactor under air at 600 °C before each activity test [33].

The photoelectron profile of Cu 2p region for all the Cu(x)CeMgAlO mixed oxides are displayed in Fig. 4a and the surface concentrations of copper together with Cu(II)/Cu atomic ratios are tabulated in Table 3. The observation of Cu 2p_{3/2} with binding energies centered at 932.2 and 934.2 eV indicates the presence of Cu⁺ and Cu²⁺ species, respectively, in all the samples [44, 45]. The shake-up satellites of Cu 2p_{3/2} emission line centered at 941.2 and 943.7 eV also confirm the presence of Cu²⁺ [45]. The existence of Cu⁺ species in the Cu(x)CeMgAlO mixed oxide catalysts suggests that, at least at the interface, CuO phase could be doped with higher valence cations, i.e. Al³⁺ and/or Ce⁴⁺, existing in the mixed oxide. The data in Table 3 show that the surface of the catalysts is enriched in Cu compared to the bulk composition (Table 2). The surface Cu(II)/Cu atomic ratio was calculated by the method developed in Ref. [45] using the following equation:

$$\% Cu(II) = \frac{B(1 + (A_{1s}/B_s))}{A + B} \times 100$$

where A is the total area of the main Cu 2p_{3/2} emission line, B is the area of the shake-up peak and A_{1s}/B_s is a factor representing the ratio of the main peak/shake-up peak areas for a 100 %

pure Cu(II) sample equal to 1.89 ± 0.08 for 20 eV pass energy [45]. The surface Cu(II)/Cu atomic ratio passes through a maximum for the Cu(15)CeMgAlO mixed oxide with increasing the Cu content, then it decreases for Cu(18)CeMgAlO sample. For the Cu(15)CeMgAlO sample calcined at different temperatures, the Cu(II)/Cu atomic ratio increases linearly with increasing the calcination temperature (Fig. S4).

The X-ray photoelectron spectra of the Ce $3d_{3/2}$ and Ce $3d_{5/2}$ core levels of the Cu(x)CeMgAlO mixed oxides are presented in Fig. 4b. The XPS spectrum of pure Ce(IV) oxide should present six peaks (three pairs of spin-orbit doublets) which are conventionally labeled in order of decreasing energy U''' , U'' , U (corresponding to the Ce $3d_{3/2}$ level) and V''' , V'' , V (corresponding to the Ce $3d_{5/2}$ level) [46]. The XPS spectrum of Ce(III) oxide should present four peaks (two pairs of spin-orbit doublets) which are labeled in order of decreasing energy U' , U^0 (corresponding to the $3d_{3/2}$ level) and V' , V^0 (corresponding to the $3d_{5/2}$ level) [46]. When both Ce(III) and Ce(IV) species are present on the surface of an oxide, the resulting spectrum is a superposition of all these ten features, as it can be seen in Fig. 4b for the Cu(x)CeMgAlO mixed oxides. The values of the characteristic binding energies of these ten features present in the XPS spectra of Ce(III) and Ce(IV) were taken from Ref. [47]. It has been reported that the U''' peak is exclusively attributed to Ce(IV), being absent from the Ce3d spectrum of pure Ce(III) oxide, and, hence, it is used as quantitative measure of the amount of Ce(IV) [48]. Thus, taking into consideration that for pure Ce(IV) oxide the U''' peak represents ca. 14 % of total integral intensity [48], the percentage of surface Ce(IV) can be calculated using the following equation:

$$\% Ce(IV) = \frac{\% U'''}{14} \times 100$$

where $\% U'''$ represents the percentage of U''' peak area with respect to the total Ce 3d area. Thus, the Ce(IV)/Ce surface atomic ratio (Table 3) is higher than 0.8 for all the mixed oxides, suggesting the presence of low quantities of surface Ce(III) that vary irrespective to the Cu content. It is worth noting that the reduction of Ce(IV) under the X-ray beam during the XPS analysis is, at least partly, responsible for the presence of surface Ce(III) species. However, for the Cu(15)CeMgAlO sample calcined at different temperatures, the Ce(IV)/Ce atomic ratio increases linearly with increasing the calcination temperature (Fig. S4). The data in Table 3 also shows that the surface Ce content is significantly lower than that of the bulk (Table 2) for all the

Cu(x)CeMgAlO mixed oxides. Taking this into consideration and the surface Cu enrichment observed, the Cu/Ce surface atomic ratio (Table 3) is significantly higher than the bulk ratio (Table 2) for all the mixed oxide samples.

The X-ray photoelectron spectra of the Al 2p and Mg 2p of the Cu(x)CeMgAlO mixed oxides are shown in Figs. S5 and S6, respectively. Fig. S6 also shows the Auger Mg KLL spectra of the Cu(x)CeMgAlO mixed oxides. The Al 2p peak appears at almost the same binding energy as Cu 3p. The relative peak positions of both Al and Mg are very stable (Table S1) and account for Al³⁺ and Mg²⁺ in their corresponding oxides. This was confirmed for Mg by calculating the modified Auger parameter (*m-AP*) using the following formula:

$$m-AP = BE_{Mg2p} + KE_{MgKLL}$$

where BE_{Mg2p} is the binding energy of Mg 2p and KE_{MgKLL} , the kinetic energy of the MgKLL peak. Indeed, the values obtained for *m-AP* (Table S1) are specific for MgO [49] in all the mixed oxide samples. The Mg/Al surface atomic ratio (Table 3) is lower than the bulk ratio for all the Cu(x)CeMgAlO mixed oxides indicating the Al enrichment of the surface.

The specific surface area, the pore volume and the pore size of the Cu(x)CeMgAlO mixed oxides are listed in Table 1 and their corresponding adsorption-desorption isotherms and pore size distributions are shown in Figs. S7 and S8, respectively. The specific surface area of the Cu-containing samples calcined at 750 °C are significantly larger than that of the CeMgAlO support and decreased with increasing Cu content from 169 m² g⁻¹ for Cu(6)CeMgAlO to 108 m² g⁻¹ for Cu(18)CeMgAlO, in line with the concurrent increase of the crystallinity of these oxides (Fig. 2a). On the other hand, as expected, the surface area of the Cu(15)CeMgAlO mixed oxide calcined at different temperatures decreases from 156 to 120 m² g⁻¹ when the calcination temperature increases from 550 to 750 °C due to the sintering of the particles. All the mixed oxide catalysts reveal type IV isotherms according to the IUPAC classification, with H3-type hysteresis loops characteristic of mesoporous materials with slit-shaped pores [50]. For both series of mixed oxides, the pore volume decreases with decreasing the surface area (Table 1). The pore size distributions for the oxides calcined at 750 °C obtained from the desorption branch of isotherms (Fig. S8) indicate bimodal pore structures extending from 3 to ca. 20 nm, with well-defined maxima at 3.7 – 3.9 nm and 7.4 – 11.5 nm, respectively. For the Cu(15)CeMgAlO samples calcined at lower temperatures larger and less well-defined bimodal pore size

distributions are observed, extending from 2 to ca. 30 nm. Thus, well-defined maxima at 3.7 and 4.1 nm are observed for the samples calcined at 650 and 550 °C, respectively, together with shoulders at ca. 9 nm for both samples (Fig. S8). This indicates that increasing the calcination temperature of the Cu(x)CeMgAl precursors from 550 to 650 °C no major textural changes take place, while increasing from 650 to 750 °C results in narrower bimodal pore structure with an increase of the large pores.

H₂-TPR measurements were carried out to investigate the reduction behavior of the different Cu(x)CeMgAlO catalysts. The TPR profiles of the mixed oxides are displayed in Fig. 5 and the corresponding H₂ consumptions are presented in Table 4. For CeMgAlO support three weak asymmetric reduction peaks were observed in the temperature ranges 230-330 °C, 330-580 °C and 580-750 °C, respectively. They account for ceria particles having different sizes or interactions with the Mg-Al mixed oxide matrix, as described elsewhere [33]. Thus, the low temperature peak was attributed to highly reducible ceria particles dispersed on the surface of the Mg(Al)O support. The medium temperature peak was attributed to ceria particles interacting with Mg(Al)O support and to Ce⁴⁺ species forming CeMgO solid solution. The high temperature peak was attributed to less reducible large ceria crystallites dispersed in the Mg(Al)O matrix. The total amount of Ce⁴⁺ species reduced was ca. 27 %. For Cu(x)CeMgAlO catalysts only one broad and intense reduction peak was observed between ca. 100 and 390 °C, with a queue extending up to a temperature going increasingly from 500 °C for Cu(6)CeMgAlO to 570 °C for Cu(18)CeMgAlO. The intensity of the peak increased with the Cu content of the catalysts. This TPR profile accounts for the reduction of both Cu²⁺ and Ce⁴⁺ species. Thus, most likely the broad and intense reduction peak can be attributed to the successive reduction of Cu²⁺ species doped in the ceria particles [51] and from well-dispersed and sintered CuO particles interacting more or less strongly with the CeMgAlO support [32] as well as to the reduction of Ce⁴⁺ species from highly reducible smaller ceria particles [52]. The weak and extended reduction signal above 390 °C can be attributed to the reduction of Ce⁴⁺ species from less reducible larger ceria particles whose reduction extends to higher and higher temperatures with increasing the ceria crystallite size, which increases with Cu content. Indeed, it has been shown that the high temperature reduction of ceria strongly depends on its crystallinity [53]. On the other hand, it is well known that the reducibility of ceria is enhanced by copper in the CuO-CeO₂ system [54, 55]. The

reduction of ceria at lower temperature in CuCeMgAlO mixed oxides compared to Cu-free CeMgAlO support is obviously due to the fact that ceria phase is reduced by atomic hydrogen formed by the dissociation of dihydrogen on the reduced copper particles [51].

The hydrogen consumption of the Cu(x)CeMgAlO catalysts is much higher compared to that of the CeMgAlO support and increases with increasing the Cu content. Assuming the total reduction of all the Cu²⁺ species in the mixed oxide, the amount of Ce⁴⁺ species reduced was calculated and is presented in Table 4. It can be observed that the amount of Ce⁴⁺ species reduced strongly decreases with increasing the Cu content in the mixed oxide. Moreover, the amount of Ce⁴⁺ species reduced exponentially decreases with increasing the ceria particle size (Fig. 6a), on one hand, and with increasing the Cu/Ce surface atomic ratio (Fig. 6b), on the other hand. These results confirm the incorporation of copper into the ceria lattice at low Cu content thus favoring the reduction of Ce⁴⁺ species, while at high Cu content, it strongly tends to agglomerate leading to separate CuO particles enriching the surface of the solid which coexist with large crystallites of ceria that are less exposed on the surface and more difficult to be reduced. Notably, the segregation of copper oxide onto ceria nanoparticles has been shown to take place for Cu molar fractions (1-x) as low as 0.1 in Ce_xCu_{1-x} nanocrystalline oxides [39].

The H₂-TPR patterns of the Cu(15)CeMgAlO systems calcined at three different temperatures, i.e. 550, 650 and 750 °C, are shown in Fig. 5b. It can be observed that the increase of the calcination temperature from 550 to 750 °C leads to a shift of the TPR peaks to lower temperature which corresponds to an increased reducibility of the samples in terms of easiness of reduction, in line with previously reported studies [56]. Regarding the hydrogen consumption (Table 4), it corresponds to the total reduction of all and of ca. 95 % Cu²⁺ species in the Cu(15)CeMgAlO samples calcined at 550 and 650 °C, respectively, therefore suggesting that no reduction of cerium takes place. Calcination at 750 °C leads not only to the total reduction of all Cu²⁺ species in the Cu(15)CeMgAlO-750 sample, but also to the reduction of a fraction of Ce⁴⁺ species. This suggests a stronger Cu-Ce interaction in the Cu(15)CeMgAlO sample calcined at 750 °C compared to the samples calcined at lower temperatures.

To obtain information about the stereochemistry and aggregation of copper in the Cu-containing mixed oxides, they were analyzed by DR-UV-Vis spectroscopy. The DR-UV-Vis spectra of all the Cu(x)CeMgAlO samples (Figure 7) show two absorption bands. The first one in the

ultraviolet region can be assigned to charge transfer transitions between copper and oxygen ions [57]. It evidences the presence of mononuclear Cu^{2+} centers (the shoulder at ca. 260 nm) as well as oligomeric $(\text{Cu}^{2+} - \text{O}^{2-} - \text{Cu}^{2+})_n^{2+}$ species (band at ca. 330 nm) [53]. The second band centered at 680-700 nm in the visible region accounts for d-d transitions characteristic for copper (II) ion in an octahedral stereochemistry [57]. The different shape of the UV-Vis spectrum of the Cu(18)CeMgAlO mixed oxide, i.e. higher intensity and a supplementary peak at ca. 450 nm, can be explained by the presence of copper (II) ions with two different stereochemistries, i.e. octahedral and square-planar, the latter corresponding to crystalline CuO, in line with the XRD data. Notably, the peak at ca. 450 nm, absent in the spectra of Cu(15)CeMgAlO-550 and Cu(15)CeMgAlO-650 samples, is also visible in the UV-Vis spectrum of the Cu(15)CeMgAlO mixed oxide calcined at 750 °C, suggesting that small CuO crystallites (with copper (II) ions in a square planar configuration) are also present in this sample, although not detected by XRD. They are obviously formed with increasing the calcination temperature.

3.2. Catalytic properties

Methane was used as a model molecule to evaluate the oxidation ability of the catalysts. Fig. 8a shows the conversion – reaction temperature plots for the Cu(x)CeMgAlO catalysts. The T_{10} , T_{50} and T_{90} temperatures, which correspond to 10, 50 and 90 % methane conversion, respectively, and both the intrinsic and specific activities at 380 °C, where the conversion level remains low for the most active catalysts, are listed in Table 5. The total oxidation activity of the Cu(x)CeMgAlO catalysts was compared to that of a reference Pd/Al₂O₃ catalyst supplied by ARPECHIM, Pitești, Romania, previously reported in Ref. [58]. The conversion – reaction temperature sigmoid for Pd/Al₂O₃ and the corresponding T_{90} value of 484 °C clearly show that this catalyst is highly active for methane combustion. In contrast, the conversion – reaction temperature sigmoid for CeMgAlO support is significantly shifted to higher temperatures (T_{90} = 637 °C) indicating its lowest activity in the series studied. The light-off sigmoids for Cu(x)CeMgAlO catalysts are between that of Pd/Al₂O₃ and CeMgAlO, indicating that copper is a key active component in methane combustion [59]. It appears that the copper content strongly influences, in a complex manner, the catalytic activity of the Cu(x)CeMgAlO catalysts. Indeed, in terms of T_{10} the catalytic activity follows the order: CeMgAlO < Cu(12)CeMgAlO <

$\text{Cu}(9)\text{CeMgAlO} < \text{Cu}(6)\text{CeMgAlO} \approx \text{Cu}(18)\text{CeMgAlO} < \text{Cu}(15)\text{CeMgAlO}$. This suggests that when Cu content ranges between 6 and 12 at. %, the effect of Cu dispersion on the catalytic activity is stronger than the effect of Cu content. This behavior has already been observed for Pd/Al₂O₃ catalysts [60]. However, regarding the T₉₀ values the order of activity appears inverted for the low Cu-content systems ($6 \leq x \leq 12$). This is obviously due to increased mass transfer limitations with increasing the surface area and decreasing the pore size when x decreases from 12 to 6 (Table 1). The most active catalyst in this series is the Cu(15)CeMgAlO mixed oxide likely due to the excellent dispersion of Cu in this material for which oligomeric (Cu²⁺– O²⁻– Cu²⁺)_n²⁺ species together with tiny not XRD-visible CuO crystallites were evidenced by UV-Vis spectroscopy (Fig. 7). Indeed, Cu(18)CeMgAlO, which contains XRD-visible crystalline CuO phase (Fig. 2), is less active than Cu(15)CeMgAlO within all the temperature range. For the latter, the T₅₀ value is ca. 100 °C lower than that of the Cu-free catalyst and remained only ca. 45 °C higher than that of the commercial Pd/Al₂O₃ catalyst. The complete conversion of methane was achieved at 600 °C (T₁₀₀) for both Cu(15)CeMgAlO and Cu(18)CeMgAlO systems, temperature which is only 30 °C higher than that corresponding to the Pd/Al₂O₃ catalyst. Both specific and intrinsic activity values calculated at 380 °C (Table 5) show a marked superiority of the Cu(15)CeMgAlO system. This behavior can be attributed not only to the excellent dispersion of copper in this catalyst, but also to a synergy effect between Cu and Ce. Indeed, the CuO-CeO₂ interactions are known to play a key role on the catalytic performance of the CuO-CeO₂ catalysts, a review paper focused on this subject being recently published [34]. Notably, this synergy effect leading to an enhanced catalytic activity in methane combustion was shown to correspond to an optimum composition in the Cu-Ce system [59]. This optimum corresponds to the Cu(15)CeMgAlO system in the studied Cu(x)CeMgAlO series.

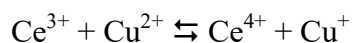
Linear correlations between the rate of methane conversion and the hydrogen consumption in H₂-TPR experiments for mixed oxides catalysts obtained from LDH precursors containing Cu [32, 58, 61] and Ce [33] have been previously evidenced. However, in the case of Cu(x)CeMgAlO systems the rate of methane transformation passes through a maximum for the Cu(15)CeMgAlO (Fig. S9) clearly suggesting that not only Cu, but also Ce is involved in catalysis, in line with the data in Table 4, with an enhanced synergy effect between these two elements for the Cu(15)CeMgAlO sample. On the other hand, the intrinsic methane conversion

rate at 380 and 400 °C and the Cu(II)/Cu surface atomic ratio follow the same trend as a function of the Cu content in the mixed oxide catalysts, with a maximum of both of them for the Cu(15)CeMgAlO system (Fig. 9). This clearly suggests that Cu(II)/Cu surface atomic ratio is a key factor controlling the catalytic activity of the Cu(x)CeMgAlO catalysts.

The presence of diffusion limitations, indicated by the decreasing slope in the Arrhenius plots (Fig. S10), can be observed at higher reaction temperatures. As a consequence, only low temperature conversion data have been used to obtain the apparent activation energies (E_a) on the different catalysts. Thus, they have been calculated from the slope of the linear part of the $\ln r_i$ versus $10^3/T$ plots in Fig. S10 and are presented in Table 5. It can be observed that the activation energy decreases when Cu is added to the CeMgAlO support to obtain Cu(6)CeMgAlO composition, then it continuously increases with increasing the Cu content in the mixed oxide catalyst. This suggests an evolution of the nature of the catalytic site, in line with the XRD and TPR results showing, on one hand, the incorporation of copper into the ceria lattice at low Cu content determining the simultaneous reduction of an important amount of Ce^{4+} species, which results in more reactive catalytic sites (lower activation energies). However, their surface density is obviously low to explain the weak catalytic activity of the catalysts with small Cu content. On the other hand, at high Cu content, separate CuO particles coexist with larger less reducible ceria crystallites and, the most likely, the less reactive catalytic site (higher activation energies) can be associated with CuO particles less interacting with CeO_2 . The high catalytic activity of the catalysts with high Cu content is due to their high density of active sites. The enhanced activity of the Cu(15)CeMgAlO system is obviously due to an excellent dispersion of CuO particles favoring their interaction with ceria, the CuO species involved in catalysis being located at CuO- CeO_2 particles interface [55, 59]. It is noteworthy that the values obtained for the E_a are in agreement with those measured for methane catalytic combustion over both similar LDH-derived CuO catalysts [32, 58, 62] and CuO- CeO_2 and CuO- ZrO_2 [55].

The calcination temperature of the precursor is known to influence the catalytic activity of the catalysts [56, 63]. Figure 8b shows the light-off curves for the total oxidation of methane over Cu(15)CeMgAlO mixed oxides catalysts calcined at 550, 650 and 750 °C. It can be observed that the sigmoid shifts to lower temperature by decreasing the calcination temperature of the catalyst, the T_{50} value ranging as follows: Cu(15)CeMgAlO-750 > Cu(15)CeMgAlO-650 >

Cu(15)CeMgAlO-550. This is in line with the surface areas of the catalysts, which decrease as the calcination temperature increases (Table 1). It is worth noting that the T_{50} and T_{100} values for the Cu(15)CeMgAlO-550 catalyst are only ca. 25 and 5 °C, respectively, higher than those of the commercial Pd/Al₂O₃ catalyst. However, in terms of intrinsic rate of CH₄ conversion (Table 5), the most active catalyst is that calcined at 750 °C in line with its lowest activation energy, the intrinsic activity ranging as follows: Cu(15)CeMgAlO-750 > Cu(15)CeMgAlO-550 > Cu(15)CeMgAlO-650. Notably, the apparent activation energy decreases with increasing the calcination temperature (Table 5), suggesting that higher calcination temperature gives rise to more reactive catalytic sites in Cu(15)CeMgAlO system within the calcination temperature range studied. This could be attributed to a strengthened Cu-Ce interaction with increasing calcination temperature as suggested by the observed increase of both Cu(II)/Cu and Ce(IV)/Ce surface atomic ratios (Fig. S4) and by the evolution of the easiness of reduction in the H₂-TPR studies. Indeed, it has been shown that the calcination process favors the Cu-Ce interaction in the mixed oxides obtained from LDH precursors [64]. This interaction results in an easier reduction of Cu²⁺ species due to synergistic involvement of the Ce⁴⁺/Ce³⁺ redox couple according to the equilibrium:



with beneficial consequences on the catalytic ability of the mixed oxide functioning via a heterogeneous redox mechanism to oxidize methane. Notably, for the catalysts calcined at different temperatures, a linear increase of the intrinsic activity with the hydrogen consumption in H₂-TPR experiments has been observed (Fig. 10). This suggests that all the reducible species evidenced in the H₂-TPR experiments are involved in the catalytic process and confirms the redox mechanism. It is noteworthy that in the CuO-CeO₂ system the optimum of the calcination temperature, studied in the range from 500 to 900 °C, was found to be 700 °C where the most stable state of Cu-Ce-O solid solution was formed [65].

Fig. 11a shows the effect of GHSV on the catalytic activity of the Cu(15)CeMgAlO mixed oxide. It can be observed that the light-off curve slightly shifts toward higher temperatures with increasing the GHSV while keeping constant the concentration of methane in the feed gas at 1 vol. %. Thus, T_{50} increases from 462 to 466 and 469 °C when the GHSV has been increased from 16000 to 20000 and 30000 h⁻¹, respectively. A shift of the light-off curve toward higher

temperatures is also observed when the concentration of methane in the feed gas has been increased from 1 to 3 vol. %, for the reaction performed over Cu(15)CeMgAlO catalyst at a constant GHSV of 16000 h^{-1} , as shown in Fig. 11b. Indeed, T_{10} and T_{50} increase from 380 to 385 and 390 °C and from 462 to 466 and 468 °C when the concentration of methane has been increased from 1 to 2 and 3 vol. %, respectively. This behavior has already been observed for a Pd/Al₂O₃ catalyst and was attributed to methane reaction orders lower than 1 [66].

It has been previously shown that both CuMgAlO [32] and CeMgAlO [33] catalysts obtained from LDH precursors display good stabilities during the complete oxidation of methane. Nevertheless, the stability of the Cu(15)CeMgAlO catalyst, the most active one in the series studied, was checked by maintaining it on stream at 550 °C for more than 50 h. Fig. 12 shows no effect of time on stream on the catalytic activity of the Cu(15)CeMgAlO catalyst suggesting its good stability, at least for the reaction conditions and the reaction time chosen.

4. Conclusion

A series of Cu(x)CeMgAlO mixed oxides with fixed Ce content of 10 at. % with respect to cations and Mg/Al mol ratio of 3, but with different copper loadings x in the range from 6 to 18 at. % were prepared by thermal decomposition at 750 °C of precursors consisting of poorly crystallized LDH and boehmite AlOOH phases. They have slit-like bimodal mesopores and relatively high surface areas, which regularly decrease from 169 to $108 \text{ m}^2 \text{ g}^{-1}$ with increasing the Cu content, and consist of periclase-like Mg(Al)O mixed oxide and CeO₂ fluorite phases, except for Cu(18)CeMgAlO, which also contains well developed CuO crystallites. At low Cu content highly dispersed Cu-doped ceria crystallites coexist with oligomeric $(\text{Cu}^{2+} - \text{O}^{2-} - \text{Cu}^{2+})_n^{2+}$ species in the Mg(Al)O matrix, while at high Cu content larger ceria crystallites less exposed on the catalyst surface coexist with separate CuO particles enriching the surface. The Cu(II)/Cu surface atomic ratio was shown to be a key factor controlling the catalytic activity of the Cu(x)CeMgAlO catalysts. With the highest Cu(II)/Cu surface atomic ratio, the Cu(15)CeMgAlO mixed oxide is the most active catalyst in this series, with a T_{50} value of only ca. 45 °C higher than that of an industrial Pd/Al₂O₃ catalyst. Its enhanced catalytic activity is attributed to an excellent dispersion of CuO, oligomeric $(\text{Cu}^{2+} - \text{O}^{2-} - \text{Cu}^{2+})_n^{2+}$ species coexisting with tiny not XRD-visible CuO crystallites strongly interacting with ceria, which leads to a strong synergy

effect between Cu and Ce. The catalytic sites are located at the CuO-CeO₂ particles interface. Decreasing the calcination temperature of the Cu(15)CeMgAl precursor from 750 to 650 and 550 °C results in mixed oxides with higher surface areas and, hence, higher catalytic activities in terms of T₅₀, which for the Cu(15)CeMgAlO-550 system is only ca. 25 °C higher than that of the industrial Pd/Al₂O₃ catalyst. However, in terms of intrinsic reaction rates the most active catalyst is that calcined at 750 °C accounting for a strengthened Cu-Ce interaction with increasing calcination temperature. A shift of the light-off curve obtained over Cu(15)CeMgAlO catalyst toward higher temperatures with increasing the methane content in the feed gas is observed accounting for methane reaction orders lower than 1. A good stability on stream of the Cu(15)CeMgAlO catalyst calcined at 750 °C was noted.

References

1. J.J. Spivey, *Ind. Eng. Chem. Res.* 26 (1987) 2165-2180.
2. W.J. Cooper, L.A. Hollway, *Nature* 384 (1996) 313-315.
3. B.J. Finlayson-Pitts, J.N. Pitts, *Science* 276 (1997) 1045-1051.
4. A.C. Lewis, N. Carslaw, P.J. Marriott, R.M. Kinghorn, P. Morrison, A.L. Lee, M.J. Pilling, *Nature* 405 (2000) 778-781.
5. M. Lopez, O.A. Sherwood, E.J. Dlugokencky, R. Kessler, L. Giroux, D.E.J. Worthy, *Atmos. Environ.* 164 (2017) 280-288.
6. D.C. Quiros, J. Smith, A. Thiruvengadam, T. Huai, S. Hu, *Atmos. Environ.* 168 (2017) 36-45.
7. J. Kirchnerova, M. Alifanti, B. Delmon, *Appl. Catal. A* 231 (2002) 65-80.
8. Y. Moro-Oka, Y. Morikawa, A. Ozaki, *J. Catal.* 7 (1967) 23-32.
9. P.O. Thevenin, P.G. Menon, S.G. Järås, *CATTECH* 7 (2003) 10-22.
10. D. Ciuparu, M.R. Lyobovsky, E. Altman, L.D. Pfefferle, A. Datye, *Catal. Rev. Sci. Eng.* 44 (2002) 593-649.
11. C. Batiot-Dupeyrat, F. Martinez-Ortega, M. Ganne, J.M. Tatibouet, *Appl. Catal. A* 206 (2001) 205-215.
12. S. Pengpanich, V. Meeyoo, T. Rirksomboon, K. Bunyakiat, *Appl. Catal. A* 234 (2002) 221-233.

13. A.Y. Zarur, J.Y. Ying, *Nature* 403 (2000) 65-67.
14. A.C. Gluhoi, N. Bogdanchikova, B.E. Nieuwenhuys, *Catal. Today* 113 (2006) 178-181.
15. T.V. Choudhary, S. Banerjee, V.R. Choudhary, *Appl. Catal. A* 234 (2002) 1-23.
16. R.A. Dalla Betta, *Catal. Today*, 35 (1997) 129-135.
17. E.C. Moretti, *Chem. Eng. Progr.* 98 (2002) 30-40.
18. R.M. Heck, R.J. Farrauto, "Catalytic Air Pollution Control. Commercial Technology",
Publisher: Van Nostrand Reinhold, New York, USA, 1995.
19. J.J. Spivey, J.B. Butt, *Catal. Today* 11 (1992) 465-500.
20. W.B. Li, J.X. Wang, H. Gong, *Catal. Today* 148 (2009) 81-87.
21. M. Tomatis, H.-H. Xu, J. He, X.-D. Zhang, *J. Chem.* (2016) Art. ID 8324826.
22. M. Shahzad Kamal, S.A. Razzak, M.M. Hossain, *Atmos. Environ.* 140 (2016) 117-134.
23. P. Kuśtrowski, A. Rokicińska, T. Kondratowicz, *Adv. Inorg. Chem.* 72 (2018) 385-419.
24. J. Chen, H. Arandiyana, X. Gao, J. Li, *Catal. Surv. Asia* 19 (2015) 140-171.
25. Z. Ma, *Curr. Catal.* 3 (2014) 15-26.
26. X.-D. Zhang, Y. Wang, Y.-Q. Yang, D. Chen, *Acta Phys. Chim. Sin.* 31 (2015) 1633-1646.
27. Y. Liu, J. Deng, S. Xie, Z. Wang, H. Dai, *Chin. J. Catal.* 37 (2016) 1193-1205.
28. P. Mohapatra, T. Mishra, K.M. Parida, *Key Eng. Mater.* 571 (2013) 71-91.
29. J. Li, M. Hu, S. Zuo, X. Wang, *Curr. Opin. Chem. Eng.* 20 (2018) 93-98.
30. I.-C. Marcu, A. Urdă, I. Popescu, V. Hulea, *in Sustainable Nanosystems Development, Properties and Applications*, M.V. Putz, M.C. Mirica (Eds.), IGI Global, Hershey, PA, USA, 2017, Ch. 3, p. 59-121.
31. S. Tanasoi, G. Mitran, N. Tanchoux, T. Cacciaguerra, F. Fajula, I. Săndulescu, D. Tichit, I.-C. Marcu, *Appl. Catal. A* 395 (2011) 78-86.
32. S. Tanasoi, N. Tanchoux, A. Urdă, D. Tichit, I. Săndulescu, F. Fajula, I.-C. Marcu, *Appl. Catal. A* 363 (2009) 135-142.
33. A. Urdă, I. Popescu, T. Cacciaguerra, N. Tanchoux, D. Tichit, I.-C. Marcu, *Appl. Catal. A* 464-465 (2013) 20-27.
34. M. Konsolakis, *Appl. Catal. B* 198 (2016) 49-66.
35. M. Piumetti, S. Bensaid, T. Andana, N. Russo, R. Pirone, D. Fino, *Appl. Catal. B* 205 (2017) 455-468.

36. P. Bera, K. R. Priolkar, P. R. Sarode, M. S. Hegde, S. Emura, R. Kumashiro, N. P. Lalla, *Chem. Mater.* 14 (2002) 3591-3601.
37. S. Hočevar, U.O. Krašovec, B. Orel, A.S. Aricó, H. Kim, *Appl. Catal. B* 28 (2000) 113-125.
38. M. Mogensen, N.M. Sammes, G.A. Tompsett, *Solid State Ionics* 129 (2000) 63-94.
39. P. Knauth, H. L. Tuller, *Solid State Ionics* 136-137 (2000) 1215-1224.
40. C. Zerva, C.J. Philippopoulos, *Appl. Catal. B* 67 (2006) 105-112.
41. B. Yildiz, L. Sun, ECS Meeting 2017, Abstract MA2017-01 1578.
42. H. Zhang, G. Zhang, X. Bi, X. Chen, *J. Mater. Chem. A* 1 (2013) 5934-5942.
43. B. Savova, D. Filkova, D. Crişan, M. Crişan, M. Răileanu, N. Drăgan, A. Galtayries, J.C. Védrine, *Appl. Catal. A* 359 (2009) 47-54.
44. P.F. Schofield, C.M.B. Henderson, S.A.T. Redfern, G. Van der Laan, *Phys. Chem. Minerals* 20 (1993) 375-381.
45. M.C. Biesinger, L.W.M. Lau, A.R. Gerson, R.St.C. Smart, *Appl. Surf. Sci.* 257 (2010) 887-898.
46. P. Burroughs, A. Hamnett, A. F. Orchard, G. Thornton, *J. Chem. Soc. Dalton Trans.* (1976) 1686-1698.
47. E. Bêche, P. Charvin, D. Perarnau, S. Abanades, G. Flamant, *Surf. Interface Anal.* 40 (2008) 264-267.
48. X. Yu, G. Li, *J. Alloy Compd* 364 (2004) 193-198.
49. NIST X-ray Photoelectron Spectroscopy Database, NIST Standard Reference Database Number 20, National Institute of Standards and Technology, Gaithersburg MD, 20899 (2000), doi:10.18434/T4T88K
50. IUPAC, Reporting physisorption data for gas/solid system, *Pure Appl. Chem.* 57 (1985) 603-619.
51. J. Beckers, G. Rothenberg, *Dalton Trans.* (2008) 6573-6578.
52. F. Giordano, A. Trovarelli, C. de Leitenburg, M. Giona, *J. Catal.* 193 (2000) 193-273.
53. S. Basag, K. Kocoł, Z. Piwowarska, M. Rutkowska, R. Baran, L. Chmielarz, *Reac. Kinet. Mech. Catal.* 121 (2017) 225-240.
54. Y. Li, Q. Fu, M. Flytzani-Stephanopoulos, *Appl. Catal. B* 27 (2000) 179-191.
55. L. Kundakovic, M. Flytzani-Stephanopoulos, *Appl. Catal. A* 171 (1998) 13-29.

56. M. Răciulete, G. Layrac, F. Papa, C. Negrilă, D. Tichit, I.-C. Marcu, *Catal. Today* 306 (2018) 276-286.
57. Lever, A.B.P. *Inorganic electronic spectroscopy*, 2nd ed.; Elsevier, Amsterdam, London, New York, 1984; pp. 553-572, ISBN 0444416994.
58. M. Răciulete, G. Layrac, D. Tichit, I.-C. Marcu, *Appl. Catal. A* 477 (2014) 195-204.
59. Y.F. Lu, F.C. Chou, F.C. Lee, C.Y. Lin, D.H. Tsai, *J. Phys. Chem. C* 120 (2016) 27389-27398.
60. B. Kucharczyk, *Polish J. Chem. Technol.* 13 (2011) 57-62.
61. I. Popescu, N. Tanchoux, D. Tichit, I.-C. Marcu, *Appl. Catal. A* 538 (2017) 81-90.
62. Z. Jiang, Z. Hao, J. Yu, H. Hou, C. Hu, J. Su, *Catal. Lett.* 99 (2005) 157-163.
63. Z.G. Liu, S.H. Chai, A. Binder, Y.Y. Li, L.T. Ji, S. Dai, *Appl. Catal. A* 451 (2013) 282-288.
64. Z. Chang, N. Zhao, J. Liu, F. Li, D.G. Evans, X. Duan, C. Forano, M. de Roy, *J. Solid State Chem.* 184 (2011) 3232-3239.
65. C.R. Jung, J. Han, S.W. Nam, T.-H. Lim, S.-A. Hong, H.-I. Lee, *Catal. Today* 93-95 (2004) 183-190.
66. Z. Yang, P. Yang, L. Zhang, M. Guoa, Y. Yan, *RSC Adv.* 4 (2014) 59418-59426.

FIGURES CAPTION

Figure 1. XRD patterns of the Cu(x)CeMgAlO precursors as prepared. Symbols: # - LDH phase; * - boehmite (AlOOH) phase.

Figure 2. XRD patterns of the Cu(x)CeMgAlO mixed oxides calcined at 750 °C (a) and of the Cu(15)CeMgAlO mixed oxides calcined at different temperatures (b). Symbols: x - CuO tenorite phase; ◆ - CeO₂ fluorite phase; ▼ - Mg(Al)O mixed oxide periclase-like phase.

Figure 3. O 1s core level (a) and C 1s core level (b) XPS spectra of the Cu(x)CeMgAlO mixed oxide catalysts: CeMgAlO (a), Cu(6)CeMgAlO (b), Cu(9)CeMgAlO (c), Cu(12)CeMgAlO (d), Cu(15)CeMgAlO (e), Cu(15)CeMgAlO-650 (f), Cu(15)CeMgAlO-550 (g), Cu(18)CeMgAlO (h).

Figure 4. Cu 2p core level (a) and Ce 3d core levels (b) XPS spectra of the Cu(x)CeMgAlO mixed oxide catalysts: Cu(6)CeMgAlO (a), Cu(9)CeMgAlO (b), Cu(12)CeMgAlO (c), Cu(15)CeMgAlO (d), Cu(15)CeMgAlO-650 (e), Cu(15)CeMgAlO-550 (f), Cu(18)CeMgAlO (g), CeMgAlO (h).

Figure 5. H₂-TPR profiles of the Cu(x)CeMgAlO mixed oxides calcined at 750 °C (a) and of the Cu(15)CeMgAlO mixed oxides calcined at different temperatures (b).

Figure 6. Amount of Ce⁴⁺ species reduced in H₂-TPR experiments vs. ceria particle size in the Cu(x)CeMgAlO mixed oxides calcined at 750 °C.

Figure 7. DR-UV-Vis spectra of the Cu(x)CeMgAlO mixed oxides: Cu(6)CeMgAlO (a), Cu(9)CeMgAlO (b), Cu(12)CeMgAlO (c), Cu(15)CeMgAlO (d), Cu(15)CeMgAlO-650 (e), Cu(15)CeMgAlO-550 (f), Cu(18)CeMgAlO (g).

Figure 8. The light-off curves for the combustion of methane over Cu(x)CeMgAlO catalysts calcined at 750 °C (a) and over Cu(15)CeMgAlO catalysts calcined at different temperatures (b) compared with that of an industrial reference Pd/Al₂O₃ catalyst. Reaction conditions: 1 vol. % methane in air, GHSV of 16000 h⁻¹, 1 cm³ of catalyst.

Figure 9. Variation of the Cu(II)/Cu surface atomic ratio and the intrinsic methane conversion rate at 380 and 400 °C as a function of the Cu content in the Cu(x)CeMgAlO mixed oxide catalysts.

Figure 10. Intrinsic activities measured at 380 °C vs. hydrogen consumption in the H₂-TPR experiments for the Cu(15)CeMgAlO catalysts calcined at different temperatures.

Figure 11. Effects of gas hourly space velocity at constant concentration of methane in the feed gas of 1 vol. % (a) and of methane concentration in the feed gas at constant GHSV of 16000 h⁻¹ (b) on methane conversion over Cu(15)CeMgAlO catalyst.

Figure 12. Conversion of methane versus time on stream for the reaction at 550 °C over Cu(15)CeMgAlO catalyst. Reaction conditions: 1 vol. % CH₄ in air and GHSV of 16000 h⁻¹, 1 cm³ of catalyst.

Cu_xCeMgAlO mixed oxide catalysts derived from multicationic LDH precursors for methane total oxidation

Hussein Mahdi S. AL-AANI¹, Emmanuel IRO², Pramodh CHIRRA², Ioana FECHETE³, Mihaela BADEA⁴, Cătălin NEGRILĂ⁵, Ionel POPESCU⁶, Maria OLEA², Ioan-Cezar MARCU^{*, 1, 6}

¹ Laboratory of Chemical Technology and Catalysis, Department of Organic Chemistry, Biochemistry and Catalysis, Faculty of Chemistry, University of Bucharest, 4-12, Blv. Regina Elisabeta, 030018, Bucharest, Romania

² School of Science, Engineering & Design, Teesside University, Middlesbrough TS1 3BX, United Kingdom

³ International Center for CVD Innovation-Nogent, Pole Technologique Sud Champagne, Université de Troyes-Antenne de Nogent, 26, rue Lavoisier, 52800 Nogent, France

⁴ Department of Inorganic Chemistry, Faculty of Chemistry, University of Bucharest, 90-92 Panduri Str., 050663, Bucharest, Romania

⁵ National Institute of Material Physics, P. O. Box MG 7, Măgurele, Romania

⁶ Research Center for Catalysts and Catalytic Processes, Faculty of Chemistry, University of Bucharest, 4-12 Blv Regina Elisabeta, 030018, Bucharest, Romania

Abstract

A series of five Cu(x)CeMgAlO mixed oxides with different copper contents (x) ranging from 6 to 18 at. % with respect to cations, but with fixed 10 at. % Ce and Mg/Al atomic ratio of 3, were prepared by thermal decomposition of layered double hydroxide (LDH) precursors at 750 °C. The solid containing 15 at. % Cu, i.e. Cu(15)CeMgAlO, was also calcined at 550 and 650 °C. Powder XRD was used to characterize the crystalline structure and SEM-EDX was used to monitor the morphology and chemical composition of both as prepared and calcined materials.

* Corresponding author. Phone: +40213051464; Fax: +40213159249; E-mail addresses: ioancezar.marcu@chimie.unibuc.ro , ioancezar_marcu@yahoo.com

Additionally, the textural properties and the reducibility of the mixed oxide catalysts were studied by nitrogen adsorption/desorption and temperature programmed reduction with hydrogen (H_2 -TPR) techniques, respectively. X-ray photoelectron spectroscopy (XPS) was used to determine the chemical state of the elements on the catalyst surface and the diffuse reflectance UV-Vis spectroscopy, to obtain information about the stereochemistry and aggregation of copper in the Cu-containing mixed oxides. Their catalytic properties in the total oxidation of methane, used as a volatile organic compound (VOC) model molecule, were evaluated and compared with those of an industrial Pd/Al₂O₃ catalyst. Their catalytic behavior was explained in correlation with their physicochemical properties. Cu(15)CeMgAlO mixed oxide was shown to be the most active catalyst in this series, with a T₅₀ (temperature corresponding to 50 % methane conversion) value of only ca. 45 °C higher than that of a commercial Pd/Al₂O₃ catalyst. This difference becomes as low as ca. 25 °C for the Cu(15)CeMgAlO system calcined at 550 °C. The influences of the contact time and of the methane concentration in the feed gas on the catalytic performances of the Cu(15)CeMgAlO catalyst have been investigated and its good stability on stream was evidenced.

Keywords: layered double hydroxides, mixed oxides catalysts, copper, cerium, methane combustion

1. Introduction

Volatile organic compounds (VOC), resulting from various industrial processes, but also from transportation and other activities, represent an important class of air pollutants [1]. Besides the direct harmful effects on human health, these compounds also contribute to the increasing of photochemical smog, formation of ground-level ozone and atmospheric ozone destruction [2-4]. Methane is a major hydrocarbon air pollutant of particular importance in global climate change, occupying the second place after carbon dioxide among the anthropogenic greenhouse gases (GHG) emitted at the global scale [5]. The Global Warming Potential (GWP) is used to compare the ability of GHG to trap heat and their persistence in the atmosphere, and methane has a GWP 25 times higher than CO₂ over a 100-year time horizon [6]. On the other hand, being the most

difficult organic molecule to oxidize due to its high stability, methane is often used as a test molecule in catalytic combustion of VOC [7].

VOC recovery from the residual gaseous effluents from different industrial processes is economically disadvantageous due to their very low concentrations and, therefore, their destruction is the only viable alternative [1, 8]. One of the main processes for the destruction of VOC is the catalytic combustion, which have some important advantages compared to traditional flame combustion [9, 10]. Thus, this process uses lower temperatures for the complete oxidation, which leads to lower energy consumption and also to the control of NO_x formation, avoiding, at the same time, the appearance of incomplete oxidation products [11-13].

The most active catalysts for VOC destruction belong to two main categories: supported noble metals and transition metal oxides [14, 15]. The supported noble metals, like Pd or Pt, are the most active catalysts for this process, which is their main advantage compared to the oxide-based catalysts [1, 16, 17]. Nevertheless, the noble metal-based catalysts have some major disadvantages: they are expensive and, because of their volatility and high sintering rates, they are easily deactivated at elevated temperatures [18]. Additionally, they may be deactivated by poisoning under the operating conditions [19]. Therefore, much effort has been made in the last years toward the design of new single and mixed transition-metal oxides catalysts to replace the noble metals for VOC abatement, a high number of research papers being published on this subject, which engendered several review papers and book chapters focusing either on catalytic combustion of VOC [20-23] and methane [24], or on different types of oxide catalysts, such as cobalt oxides [25], mesoporous silica-supported catalysts [26], ordered porous transition metal oxides [27], pillared clays [28, 29] and layered double hydroxide-derived mixed oxides [30].

Among the transition-metal mixed oxides, those obtained from layered double hydroxides (LDH) precursors were proven to have great potential as combustion catalysts, as they have high specific surface areas, high thermal stability and tunable redox and acid-base properties [30]. Indeed, it has been shown that mesoporous MMgAlO mixed oxide catalysts (M = Mn, Fe, Co, Ni, Cu, Zn, Ag and Pd), obtained by thermal decomposition of LDH precursors, are promising catalysts for the total oxidation of short-chain hydrocarbons [31]. Among the non-noble metal-containing catalysts, the Cu-containing system has been shown to be the most active in methane combustion, being also highly stable in the reaction conditions. Its catalytic activity depends on

the Cu content, the optimum being of ca. 12 at. % Cu and corresponds to the best dispersion of the copper-containing species in the MgAlO matrix [32]. On the other hand, from a series of lanthanide-containing LDH-derived mixed oxides catalysts, LnMgAlO (Ln = Ce, Sm, Dy and Yb), the Ce-containing one turned out to be the most active in methane combustion, the optimum content being ca. 10 at. % Ce [33]. Therefore, in an attempt to converge the benefits of preparation of mixed oxides from LDH precursors with the high activity of Cu-based systems in methane combustion and taking into consideration an expected Cu-Ce synergistic effect [34, 35], the present work investigates a series of new LDH-derived Cu-Ce-MgAl mixed oxides with 10 at. % Ce and different Cu content ranging from 6 to 18 at. %.

2. Experimental section

2.1. Catalysts preparation

A series of five Cu(x)CeMgAl LDH precursors with different copper contents ranging from 6 to 18 at. % with respect to cations, but with fixed 10 at. % Ce and Mg/Al atomic ratio of 3, were prepared by coprecipitation under ambient atmosphere. In a typical procedure, a mixed salts solution (200 mL) of Mg(NO₃)₂·6H₂O, Al(NO₃)₃·9H₂O and Cu(NO₃)₂·3H₂O and an alkaline solution of NaOH (2 M) were simultaneously added dropwise into a beaker containing 200 mL of cerium nitrate solution (Ce(NO₃)₃·6H₂O) at room temperature with controlled rate to maintain the pH close to 10. After complete precipitation, the slurry was aged at 80 °C overnight under vigorous stirring. The suspension was then separated by centrifugation, washed with deionized water and finally dried overnight at 80 °C. The Cu(x)CeMgAlO catalysts (with x = 6, 9, 12, 15 and 18 at. %, respectively) were obtained by calcination of their corresponding LDH precursors in air at 750 °C for 8 h. The Cu-free CeMgAl LDH precursor and the corresponding CeMgAlO mixed oxide were obtained following the same protocol.

In order to investigate the influence of the calcination temperature on the catalytic properties of the mixed oxides, the Cu(15)CeMgAl LDH precursor was also calcined at 550 and 650 °C, the resulting mixed oxides being noted Cu(15)CeMgAlO-550 and Cu(15)CeMgAlO-650, respectively.

2.2. Catalysts characterization

Powder X-ray diffraction (XRD) patterns of both precursors and mixed oxides were recorded on a Siemens D500 powder X-ray diffractometer with Bragg-Brentano geometry using nickel-filtered Cu-K α radiation ($\lambda = 0.15406$ nm). They were recorded over the 5-70° 2 θ angular range at a scanning rate of 1° min⁻¹. Crystalline phases were identified using standard JCPDS files.

Scanning electron microscopy (SEM) together with X-ray energy dispersion analysis (EDX) were used to monitor the morphology and chemical composition of both precursors and mixed oxides. SEM/EDX examination was performed using a Hitachi S-3400N microscope operated at an accelerating voltage of 20 kV. Four different points were analyzed on each sample.

X-ray photoelectron spectroscopy (XPS) was employed to determine the chemical state of the elements on the catalyst surface with a SPECS spectrometer equipped with a PHOIBOS 150 analyzer using a monochromatic Al K α radiation source (1486.7 eV). The acquisition was operated at a pass energy of 20 eV for the individual spectral lines and 50 eV for the extended spectra. The analysis of the spectra has been performed with the Spectral Data Processor v2.3 software using Voigt functions and usual sensitivity factors.

The textural characterization was performed using the conventional nitrogen adsorption/desorption method, with a Micromeritics ASAP 2010 automatic equipment. The surface areas were calculated using the BET method in the relative pressure, P/P_0 , region 0.065-0.2, while the pore sizes were determined by the BJH method from the nitrogen desorption branch. Prior to nitrogen adsorption, the oxide samples were degassed at 300 °C for 12 h.

The reducibility of the catalysts was studied by temperature programmed reduction under hydrogen (H₂-TPR). Experiments were performed using a CATLAB microreactor – MS system (Hiden Analytical, UK) under a flow of 5 % H₂ in Ar mixture (flowrate 30 mL min⁻¹) through the CATLAB's packed micro-reactor (4 mm internal diameter and length 18.5 cm) containing about 35 mg of sample, which was heated at a constant rate of 10 °C min⁻¹ up to 800 °C. The system was maintained for 1 h at 800 °C under H₂/Ar flow to complete the reduction.

Diffuse reflectance UV-Vis spectra were recorded in the range 200-1300 nm, using Spectralon as a standard, in a Jasco V 670 spectrophotometer. The obtained reflectance spectra were converted into the dependencies of Kubelka-Munk function on the absorption energy.

2.3. Catalytic test

The catalytic tests for the methane combustion over the mixed oxide catalysts were carried out in a fixed bed quartz tube down-flow reactor at atmospheric pressure. If not otherwise specified, a mixture of CH₄ and air containing 1 vol. % methane was passed through 1 cm³ (ca. 0.9 g) catalyst bed with a total flow rate of 267 mL min⁻¹ corresponding to a gas hourly space velocity (GHSV) of 16000 h⁻¹. For comparison, an industrially used Pd/Al₂O₃ catalyst (supplied by ARPECHIM Pitești, Romania) was tested in methane combustion in similar conditions, with a GHSV of 20000 h⁻¹. Before testing, the catalyst was pre-treated for 30 min in a stream of nitrogen at 600 °C (500°C for the sample calcined at 550 °C) for cleaning its surface. After pre-treatment, the catalyst was cooled down to 300 °C and the reaction was started by introducing the reaction mixture. Activity measurements were performed by increasing the reaction temperature from 300 to 650 °C at regular intervals. The reactants and product gases were analyzed on-line by a Clarus 500 Gas-Chromatograph equipped with a thermal conductivity detector, using two packed columns in series (6 ft Hayesep and 10 ft molecular sieve 5 Å). The catalysts activity was characterized by T₁₀, T₅₀ and T₉₀ representing the temperatures of methane conversions of 10, 50 and 90 %, respectively. The conversion was calculated as the amount of methane transformed in the reaction divided by the amount that was fed to the reactor by using the following formula:

$$\text{Conversion (\%)} = \frac{C_{CH_4,in} - C_{CH_4,out}}{C_{CH_4,in}} \times 100$$

where $C_{CH_4,in}$ and $C_{CH_4,out}$ represent the methane concentration (v/v) in the feed and effluent gases, respectively.

Complete selectivity to CO₂ and H₂O was always observed. The carbon balance was calculated based on the following equation:

$$C_{CH_4,in} = C_{CH_4,out} + C_{CO_2,out}$$

where $C_{CO_2,out}$ is the concentration of carbon dioxide (v/v) in the effluent gas. It was satisfactory in all runs to within ± 2 %.

3. Results and discussion

3.1. Catalysts characterization

The XRD patterns of the as-prepared precursor samples are displayed in Fig. 1. It can be observed that all the precursors consist of poorly crystallized LDH (JCPDS 37-0630) and boehmite AlOOH (JCPDS 83-2384) phases. The absence of diffraction lines corresponding to copper- or cerium-containing additional phases can be noted suggesting that these cations are well dispersed in the precursor samples.

For all the Cu(x)CeMgAlO catalysts, Mg(Al)O mixed oxide phase with the periclase-like structure (JCPDS-ICDD4-0829) and CeO₂ fluorite phase (JCPDS 75-0076) were identified (Fig. 2a). Except for Cu(18)CeMgAlO system, no diffraction lines corresponding to CuO phase were observed suggesting that copper is well dispersed in the Cu(x)CeMgAlO catalysts with x < 18.

Unexpectedly, the value of the lattice parameter, *d*, of the fluorite structure of the ceria phase calculated using the Bragg's law, from the three most intense lines in the diffractograms, i.e. (111), (220) and (311), increases with increasing Cu content in the Cu(x)CeMgAlO catalysts (Table 1). Indeed, taking into consideration that the radius of Cu²⁺ ion is lower than that of Ce⁴⁺, and those of Cu⁺ and Ce⁴⁺ ions are similar, the lattice parameter should decrease with increasing Cu content [36, 37]. Compared to the theoretical value of the ceria lattice parameter of 0.5411 nm [38], that of the samples with x < 12 is lower, and that of the samples with x ≥ 12 is even higher. This suggests the incorporation of copper into the ceria lattice at low Cu content, while at high Cu content ceria crystallites coexist with separate CuO particles, the latter being well developed in the Cu(18)CeMgAlO mixed oxide, in line with its XRD pattern. This is in agreement with the observed decrease of Cu solubility in ceria with increasing the grain size of the latter, resulting in the segregation of copper to the grain boundaries [39].

The full-width at half-maximum (FWHM) of the three most intense reflections of CeO₂ phase allows estimating the average crystallite size using the Debye-Scherrer equation:

$$D \approx \frac{1.08\lambda}{(2\theta)_{FWHM} \cos \theta}$$

where *D* is the crystallite size, *λ* is the wavelength of the Cu K-alpha radiation (0.15406 nm), *θ* is the Bragg diffraction angle. They are presented in Table 1. It can be observed that the crystallite size of ceria continuously increases with increasing the Cu content in the catalyst from 6.3 nm for Cu(6)CeMgAlO to 15.1 nm for Cu(18)CeMgAlO. A similar behavior has already been observed for coprecipitated CuO-CeO₂ mixed oxides [40].

Taking into consideration that the Ce content is almost constant in all the mixed oxide samples, it can be concluded that at low Cu content highly dispersed Cu-doped ceria crystallites are formed in the Mg(Al)O matrix, while at high Cu content larger ceria crystallites coexist with CuO particles that form a separate phase identified by XRD in the Cu(18)CeMgAlO mixed oxide. This reflects the low solubility of Cu ions in ceria [41].

The effect of calcination temperature on the XRD pattern of the Cu(15)CeMgAlO mixed oxide is shown on Fig. 2b. It can be observed that the diffraction lines of both Mg(Al)O mixed oxide and CeO₂ fluorite phases become significantly larger when the calcination temperature decreases from 750 to 650 °C suggesting a strong decrease of the crystallite size. Indeed, the average crystallite size of ceria decreases from 12.2 nm for the sample calcined at 750 °C to 4.1 nm for that calcined at 650 °C (Table 1). Further decreasing the calcination temperature from 650 to 550 °C results in slightly larger and less intense diffraction lines accounting for a lower crystallinity of the sample Cu(15)CeMgAlO-550. The average crystallite size of ceria slightly decreases from 4.1 nm for Cu(15)CeMgAlO-650 to 3.1 nm for Cu(15)CeMgAlO-550 (Table 1).

It is worth noting that the XRD patterns of the catalysts remain unchanged after the catalytic tests as it can be observed in Fig. S1 for the Cu(x)CeMgAlO samples with $x = 6, 12$ and 18, respectively.

The cationic composition of both LDH precursors and calcined oxide catalysts has been determined by EDX spectroscopy and it is tabulated in Table 2. It can be observed that in both as-prepared and calcined samples the cationic content is close to the theoretical values within the limits of experimental error of the method used. The Mg/Al atomic ratio was very close to the fixed value of 3, while the Cu/Ce atomic ratio was slightly higher than the fixed value.

The SEM micrographs of both as-prepared and calcined Cu(x)CeMgAl samples are shown in Fig. S2. It can be observed that there are no significant differences between the particle morphologies of the precursors, on one hand, and of the calcined oxides, on the other hand. More unexpected, no significant differences can be observed between the particle morphologies of the precursors and of the corresponding mixed oxides. This indicates that neither the Cu content within the range 6-18 at. %, nor the calcination temperature up to 750 °C influence the particle morphology of the studied materials.

X-ray photoelectron spectroscopy (XPS) has been used to investigate the oxidation states of the different elements and the surface composition of the Cu(x)CeMgAlO mixed oxides. All the expected elements, i.e. Cu, Ce, Mg, Al, O and C are present on their surface (Table 3). The O 1s core level XPS spectra (Fig. 3a) showed for all the samples a peak deconvoluted into two components which could be related to lattice oxygen in oxide (BE ca. 529.7 eV) and oxygen in the lateral structure (BE ca. 531.6 eV), respectively [42]. The oxygen in the lateral structure corresponds to hydroxyl and/or carbonate species [43] and also to subsurface oxygen ions with particular coordination and lower electron density than the lattice oxygen [42]. The component at 531.6 eV obviously accounts for the hydroxylation and carbonatation of the catalyst surface, as its relative intensity increased linearly with the specific surface area of the catalyst (Fig. S3), except for Cu(18)CeMgAlO sample. For the latter, the subsurface oxygen ions with particular coordination, probably located at the interface of the crystalline CuO and CeO₂ phases, also have an important contribution to the XPS peak at 531.6 eV. The C 1s core level (Fig. 3b) shows two main contributions: the adventitious hydrocarbon species (BE 284.8 eV) and carbon in carbonate (BE ca. 289.2 eV) [43]. These results confirm the need of pretreating the catalysts in the reactor under air at 600 °C before each activity test [33].

The photoelectron profile of Cu 2p region for all the Cu(x)CeMgAlO mixed oxides are displayed in Fig. 4a and the surface concentrations of copper together with Cu(II)/Cu atomic ratios are tabulated in Table 3. The observation of Cu 2p_{3/2} with binding energies centered at 932.2 and 934.2 eV indicates the presence of Cu⁺ and Cu²⁺ species, respectively, in all the samples [44, 45]. The shake-up satellites of Cu 2p_{3/2} emission line centered at 941.2 and 943.7 eV also confirm the presence of Cu²⁺ [45]. The existence of Cu⁺ species in the Cu(x)CeMgAlO mixed oxide catalysts suggests that, at least at the interface, CuO phase could be doped with higher valence cations, i.e. Al³⁺ and/or Ce⁴⁺, existing in the mixed oxide. The data in Table 3 show that the surface of the catalysts is enriched in Cu compared to the bulk composition (Table 2). The surface Cu(II)/Cu atomic ratio was calculated by the method developed in Ref. [45] using the following equation:

$$\% Cu(II) = \frac{B(1 + (A_{1s}/B_s))}{A + B} \times 100$$

where A is the total area of the main Cu 2p_{3/2} emission line, B is the area of the shake-up peak and A_{1s}/B_s is a factor representing the ratio of the main peak/shake-up peak areas for a 100 %

pure Cu(II) sample equal to 1.89 ± 0.08 for 20 eV pass energy [45]. The surface Cu(II)/Cu atomic ratio passes through a maximum for the Cu(15)CeMgAlO mixed oxide with increasing the Cu content, then it decreases for Cu(18)CeMgAlO sample. For the Cu(15)CeMgAlO sample calcined at different temperatures, the Cu(II)/Cu atomic ratio increases linearly with increasing the calcination temperature (Fig. S4).

The X-ray photoelectron spectra of the Ce $3d_{3/2}$ and Ce $3d_{5/2}$ core levels of the Cu(x)CeMgAlO mixed oxides are presented in Fig. 4b. The XPS spectrum of pure Ce(IV) oxide should present six peaks (three pairs of spin-orbit doublets) which are conventionally labeled in order of decreasing energy U''' , U'' , U (corresponding to the Ce $3d_{3/2}$ level) and V''' , V'' , V (corresponding to the Ce $3d_{5/2}$ level) [46]. The XPS spectrum of Ce(III) oxide should present four peaks (two pairs of spin-orbit doublets) which are labeled in order of decreasing energy U' , U^0 (corresponding to the $3d_{3/2}$ level) and V' , V^0 (corresponding to the $3d_{5/2}$ level) [46]. When both Ce(III) and Ce(IV) species are present on the surface of an oxide, the resulting spectrum is a superposition of all these ten features, as it can be seen in Fig. 4b for the Cu(x)CeMgAlO mixed oxides. The values of the characteristic binding energies of these ten features present in the XPS spectra of Ce(III) and Ce(IV) were taken from Ref. [47]. It has been reported that the U''' peak is exclusively attributed to Ce(IV), being absent from the Ce3d spectrum of pure Ce(III) oxide, and, hence, it is used as quantitative measure of the amount of Ce(IV) [48]. Thus, taking into consideration that for pure Ce(IV) oxide the U''' peak represents ca. 14 % of total integral intensity [48], the percentage of surface Ce(IV) can be calculated using the following equation:

$$\% Ce(IV) = \frac{\% U'''}{14} \times 100$$

where $\% U'''$ represents the percentage of U''' peak area with respect to the total Ce 3d area. Thus, the Ce(IV)/Ce surface atomic ratio (Table 3) is higher than 0.8 for all the mixed oxides, suggesting the presence of low quantities of surface Ce(III) that vary irrespective to the Cu content. It is worth noting that the reduction of Ce(IV) under the X-ray beam during the XPS analysis is, at least partly, responsible for the presence of surface Ce(III) species. However, for the Cu(15)CeMgAlO sample calcined at different temperatures, the Ce(IV)/Ce atomic ratio increases linearly with increasing the calcination temperature (Fig. S4). The data in Table 3 also shows that the surface Ce content is significantly lower than that of the bulk (Table 2) for all the

Cu(x)CeMgAlO mixed oxides. Taking this into consideration and the surface Cu enrichment observed, the Cu/Ce surface atomic ratio (Table 3) is significantly higher than the bulk ratio (Table 2) for all the mixed oxide samples.

The X-ray photoelectron spectra of the Al 2p and Mg 2p of the Cu(x)CeMgAlO mixed oxides are shown in Figs. S5 and S6, respectively. Fig. S6 also shows the Auger Mg KLL spectra of the Cu(x)CeMgAlO mixed oxides. The Al 2p peak appears at almost the same binding energy as Cu 3p. The relative peak positions of both Al and Mg are very stable (Table S1) and account for Al³⁺ and Mg²⁺ in their corresponding oxides. This was confirmed for Mg by calculating the modified Auger parameter (*m-AP*) using the following formula:

$$m-AP = BE_{Mg2p} + KE_{MgKLL}$$

where BE_{Mg2p} is the binding energy of Mg 2p and KE_{MgKLL} , the kinetic energy of the MgKLL peak. Indeed, the values obtained for *m-AP* (Table S1) are specific for MgO [49] in all the mixed oxide samples. The Mg/Al surface atomic ratio (Table 3) is lower than the bulk ratio for all the Cu(x)CeMgAlO mixed oxides indicating the Al enrichment of the surface.

The specific surface area, the pore volume and the pore size of the Cu(x)CeMgAlO mixed oxides are listed in Table 1 and their corresponding adsorption-desorption isotherms and pore size distributions are shown in Figs. S7 and S8, respectively. The specific surface area of the Cu-containing samples calcined at 750 °C are significantly larger than that of the CeMgAlO support and decreased with increasing Cu content from 169 m² g⁻¹ for Cu(6)CeMgAlO to 108 m² g⁻¹ for Cu(18)CeMgAlO, in line with the concurrent increase of the crystallinity of these oxides (Fig. 2a). On the other hand, as expected, the surface area of the Cu(15)CeMgAlO mixed oxide calcined at different temperatures decreases from 156 to 120 m² g⁻¹ when the calcination temperature increases from 550 to 750 °C due to the sintering of the particles. All the mixed oxide catalysts reveal type IV isotherms according to the IUPAC classification, with H3-type hysteresis loops characteristic of mesoporous materials with slit-shaped pores [50]. For both series of mixed oxides, the pore volume decreases with decreasing the surface area (Table 1). The pore size distributions for the oxides calcined at 750 °C obtained from the desorption branch of isotherms (Fig. S8) indicate bimodal pore structures extending from 3 to ca. 20 nm, with well-defined maxima at 3.7 – 3.9 nm and 7.4 – 11.5 nm, respectively. For the Cu(15)CeMgAlO samples calcined at lower temperatures larger and less well-defined bimodal pore size

distributions are observed, extending from 2 to ca. 30 nm. Thus, well-defined maxima at 3.7 and 4.1 nm are observed for the samples calcined at 650 and 550 °C, respectively, together with shoulders at ca. 9 nm for both samples (Fig. S8). This indicates that increasing the calcination temperature of the Cu(x)CeMgAl precursors from 550 to 650 °C no major textural changes take place, while increasing from 650 to 750 °C results in narrower bimodal pore structure with an increase of the large pores.

H₂-TPR measurements were carried out to investigate the reduction behavior of the different Cu(x)CeMgAlO catalysts. The TPR profiles of the mixed oxides are displayed in Fig. 5 and the corresponding H₂ consumptions are presented in Table 4. For CeMgAlO support three weak asymmetric reduction peaks were observed in the temperature ranges 230-330 °C, 330-580 °C and 580-750 °C, respectively. They account for ceria particles having different sizes or interactions with the Mg-Al mixed oxide matrix, as described elsewhere [33]. Thus, the low temperature peak was attributed to highly reducible ceria particles dispersed on the surface of the Mg(Al)O support. The medium temperature peak was attributed to ceria particles interacting with Mg(Al)O support and to Ce⁴⁺ species forming CeMgO solid solution. The high temperature peak was attributed to less reducible large ceria crystallites dispersed in the Mg(Al)O matrix. The total amount of Ce⁴⁺ species reduced was ca. 27 %. For Cu(x)CeMgAlO catalysts only one broad and intense reduction peak was observed between ca. 100 and 390 °C, with a queue extending up to a temperature going increasingly from 500 °C for Cu(6)CeMgAlO to 570 °C for Cu(18)CeMgAlO. The intensity of the peak increased with the Cu content of the catalysts. This TPR profile accounts for the reduction of both Cu²⁺ and Ce⁴⁺ species. Thus, most likely the broad and intense reduction peak can be attributed to the successive reduction of Cu²⁺ species doped in the ceria particles [51] and from well-dispersed and sintered CuO particles interacting more or less strongly with the CeMgAlO support [32] as well as to the reduction of Ce⁴⁺ species from highly reducible smaller ceria particles [52]. The weak and extended reduction signal above 390 °C can be attributed to the reduction of Ce⁴⁺ species from less reducible larger ceria particles whose reduction extends to higher and higher temperatures with increasing the ceria crystallite size, which increases with Cu content. Indeed, it has been shown that the high temperature reduction of ceria strongly depends on its crystallinity [53]. On the other hand, it is well known that the reducibility of ceria is enhanced by copper in the CuO-CeO₂ system [54, 55]. The

reduction of ceria at lower temperature in CuCeMgAlO mixed oxides compared to Cu-free CeMgAlO support is obviously due to the fact that ceria phase is reduced by atomic hydrogen formed by the dissociation of dihydrogen on the reduced copper particles [51].

The hydrogen consumption of the Cu(x)CeMgAlO catalysts is much higher compared to that of the CeMgAlO support and increases with increasing the Cu content. Assuming the total reduction of all the Cu²⁺ species in the mixed oxide, the amount of Ce⁴⁺ species reduced was calculated and is presented in Table 4. It can be observed that the amount of Ce⁴⁺ species reduced strongly decreases with increasing the Cu content in the mixed oxide. Moreover, the amount of Ce⁴⁺ species reduced exponentially decreases with increasing the ceria particle size (Fig. 6a), on one hand, and with increasing the Cu/Ce surface atomic ratio (Fig. 6b), on the other hand. These results confirm the incorporation of copper into the ceria lattice at low Cu content thus favoring the reduction of Ce⁴⁺ species, while at high Cu content, it strongly tends to agglomerate leading to separate CuO particles enriching the surface of the solid which coexist with large crystallites of ceria that are less exposed on the surface and more difficult to be reduced. Notably, the segregation of copper oxide onto ceria nanoparticles has been shown to take place for Cu molar fractions (1-x) as low as 0.1 in Ce_xCu_{1-x} nanocrystalline oxides [39].

The H₂-TPR patterns of the Cu(15)CeMgAlO systems calcined at three different temperatures, i.e. 550, 650 and 750 °C, are shown in Fig. 5b. It can be observed that the increase of the calcination temperature from 550 to 750 °C leads to a shift of the TPR peaks to lower temperature which corresponds to an increased reducibility of the samples in terms of easiness of reduction, in line with previously reported studies [56]. Regarding the hydrogen consumption (Table 4), it corresponds to the total reduction of all and of ca. 95 % Cu²⁺ species in the Cu(15)CeMgAlO samples calcined at 550 and 650 °C, respectively, therefore suggesting that no reduction of cerium takes place. Calcination at 750 °C leads not only to the total reduction of all Cu²⁺ species in the Cu(15)CeMgAlO-750 sample, but also to the reduction of a fraction of Ce⁴⁺ species. This suggests a stronger Cu-Ce interaction in the Cu(15)CeMgAlO sample calcined at 750 °C compared to the samples calcined at lower temperatures.

To obtain information about the stereochemistry and aggregation of copper in the Cu-containing mixed oxides, they were analyzed by DR-UV-Vis spectroscopy. The DR-UV-Vis spectra of all the Cu(x)CeMgAlO samples (Figure 7) show two absorption bands. The first one in the

ultraviolet region can be assigned to charge transfer transitions between copper and oxygen ions [57]. It evidences the presence of mononuclear Cu^{2+} centers (the shoulder at ca. 260 nm) as well as oligomeric $(\text{Cu}^{2+} - \text{O}^{2-} - \text{Cu}^{2+})_n^{2+}$ species (band at ca. 330 nm) [53]. The second band centered at 680-700 nm in the visible region accounts for d-d transitions characteristic for copper (II) ion in an octahedral stereochemistry [57]. The different shape of the UV-Vis spectrum of the Cu(18)CeMgAlO mixed oxide, i.e. higher intensity and a supplementary peak at ca. 450 nm, can be explained by the presence of copper (II) ions with two different stereochemistries, i.e. octahedral and square-planar, the latter corresponding to crystalline CuO, in line with the XRD data. Notably, the peak at ca. 450 nm, absent in the spectra of Cu(15)CeMgAlO-550 and Cu(15)CeMgAlO-650 samples, is also visible in the UV-Vis spectrum of the Cu(15)CeMgAlO mixed oxide calcined at 750 °C, suggesting that small CuO crystallites (with copper (II) ions in a square planar configuration) are also present in this sample, although not detected by XRD. They are obviously formed with increasing the calcination temperature.

3.2. Catalytic properties

Methane was used as a model molecule to evaluate the oxidation ability of the catalysts. Fig. 8a shows the conversion – reaction temperature plots for the Cu(x)CeMgAlO catalysts. The T_{10} , T_{50} and T_{90} temperatures, which correspond to 10, 50 and 90 % methane conversion, respectively, and both the intrinsic and specific activities at 380 °C, where the conversion level remains low for the most active catalysts, are listed in Table 5. The total oxidation activity of the Cu(x)CeMgAlO catalysts was compared to that of a reference Pd/Al₂O₃ catalyst supplied by ARPECHIM, Pitești, Romania, previously reported in Ref. [58]. The conversion – reaction temperature sigmoid for Pd/Al₂O₃ and the corresponding T_{90} value of 484 °C clearly show that this catalyst is highly active for methane combustion. In contrast, the conversion – reaction temperature sigmoid for CeMgAlO support is significantly shifted to higher temperatures (T_{90} = 637 °C) indicating its lowest activity in the series studied. The light-off sigmoids for Cu(x)CeMgAlO catalysts are between that of Pd/Al₂O₃ and CeMgAlO, indicating that copper is a key active component in methane combustion [59]. It appears that the copper content strongly influences, in a complex manner, the catalytic activity of the Cu(x)CeMgAlO catalysts. Indeed, in terms of T_{10} the catalytic activity follows the order: CeMgAlO < Cu(12)CeMgAlO <

$\text{Cu}(9)\text{CeMgAlO} < \text{Cu}(6)\text{CeMgAlO} \approx \text{Cu}(18)\text{CeMgAlO} < \text{Cu}(15)\text{CeMgAlO}$. This suggests that when Cu content ranges between 6 and 12 at. %, the effect of Cu dispersion on the catalytic activity is stronger than the effect of Cu content. This behavior has already been observed for Pd/Al₂O₃ catalysts [60]. However, regarding the T₉₀ values the order of activity appears inverted for the low Cu-content systems ($6 \leq x \leq 12$). This is obviously due to increased mass transfer limitations with increasing the surface area and decreasing the pore size when x decreases from 12 to 6 (Table 1). The most active catalyst in this series is the Cu(15)CeMgAlO mixed oxide likely due to the excellent dispersion of Cu in this material for which oligomeric (Cu²⁺– O²⁻– Cu²⁺)_n²⁺ species together with tiny not XRD-visible CuO crystallites were evidenced by UV-Vis spectroscopy (Fig. 7). Indeed, Cu(18)CeMgAlO, which contains XRD-visible crystalline CuO phase (Fig. 2), is less active than Cu(15)CeMgAlO within all the temperature range. For the latter, the T₅₀ value is ca. 100 °C lower than that of the Cu-free catalyst and remained only ca. 45 °C higher than that of the commercial Pd/Al₂O₃ catalyst. **The complete conversion of methane was achieved at 600 °C (T₁₀₀) for both Cu(15)CeMgAlO and Cu(18)CeMgAlO systems, temperature which is only 30 °C higher than that corresponding to the Pd/Al₂O₃ catalyst.** Both specific and intrinsic activity values calculated at 380 °C (Table 5) show a marked superiority of the Cu(15)CeMgAlO system. This behavior can be attributed not only to the excellent dispersion of copper in this catalyst, but also to a synergy effect between Cu and Ce. Indeed, the CuO–CeO₂ interactions are known to play a key role on the catalytic performance of the CuO–CeO₂ catalysts, a review paper focused on this subject being recently published [34]. Notably, this synergy effect leading to an enhanced catalytic activity in methane combustion was shown to correspond to an optimum composition in the Cu–Ce system [59]. This optimum corresponds to the Cu(15)CeMgAlO system in the studied Cu(x)CeMgAlO series.

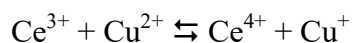
Linear correlations between the rate of methane conversion and the hydrogen consumption in H₂-TPR experiments for mixed oxides catalysts obtained from LDH precursors containing Cu [32, 58, 61] and Ce [33] have been previously evidenced. However, in the case of Cu(x)CeMgAlO systems the rate of methane transformation passes through a maximum for the Cu(15)CeMgAlO (Fig. S9) clearly suggesting that not only Cu, but also Ce is involved in catalysis, in line with the data in Table 4, with an enhanced synergy effect between these two elements for the Cu(15)CeMgAlO sample. On the other hand, the intrinsic methane conversion

rate at 380 and 400 °C and the Cu(II)/Cu surface atomic ratio follow the same trend as a function of the Cu content in the mixed oxide catalysts, with a maximum of both of them for the Cu(15)CeMgAlO system (Fig. 9). This clearly suggests that Cu(II)/Cu surface atomic ratio is a key factor controlling the catalytic activity of the Cu(x)CeMgAlO catalysts.

The presence of diffusion limitations, indicated by the decreasing slope in the Arrhenius plots (Fig. S10), can be observed at higher reaction temperatures. As a consequence, only low temperature conversion data have been used to obtain the apparent activation energies (E_a) on the different catalysts. Thus, they have been calculated from the slope of the linear part of the $\ln r_i$ versus $10^3/T$ plots in Fig. S10 and are presented in Table 5. It can be observed that the activation energy decreases when Cu is added to the CeMgAlO support to obtain Cu(6)CeMgAlO composition, then it continuously increases with increasing the Cu content in the mixed oxide catalyst. This suggests an evolution of the nature of the catalytic site, in line with the XRD and TPR results showing, on one hand, the incorporation of copper into the ceria lattice at low Cu content determining the simultaneous reduction of an important amount of Ce^{4+} species, which results in more reactive catalytic sites (lower activation energies). However, their surface density is obviously low to explain the weak catalytic activity of the catalysts with small Cu content. On the other hand, at high Cu content, separate CuO particles coexist with larger less reducible ceria crystallites and, the most likely, the less reactive catalytic site (higher activation energies) can be associated with CuO particles less interacting with CeO_2 . The high catalytic activity of the catalysts with high Cu content is due to their high density of active sites. The enhanced activity of the Cu(15)CeMgAlO system is obviously due to an excellent dispersion of CuO particles favoring their interaction with ceria, the CuO species involved in catalysis being located at CuO- CeO_2 particles interface [55, 59]. It is noteworthy that the values obtained for the E_a are in agreement with those measured for methane catalytic combustion over both similar LDH-derived CuO catalysts [32, 58, 62] and CuO- CeO_2 and CuO- ZrO_2 [55].

The calcination temperature of the precursor is known to influence the catalytic activity of the catalysts [56, 63]. Figure 8b shows the light-off curves for the total oxidation of methane over Cu(15)CeMgAlO mixed oxides catalysts calcined at 550, 650 and 750 °C. It can be observed that the sigmoid shifts to lower temperature by decreasing the calcination temperature of the catalyst, the T_{50} value ranging as follows: Cu(15)CeMgAlO-750 > Cu(15)CeMgAlO-650 >

Cu(15)CeMgAlO-550. This is in line with the surface areas of the catalysts, which decrease as the calcination temperature increases (Table 1). It is worth noting that the T_{50} and T_{100} values for the Cu(15)CeMgAlO-550 catalyst are only ca. 25 and 5 °C, respectively, higher than those of the commercial Pd/Al₂O₃ catalyst. However, in terms of intrinsic rate of CH₄ conversion (Table 5), the most active catalyst is that calcined at 750 °C in line with its lowest activation energy, the intrinsic activity ranging as follows: Cu(15)CeMgAlO-750 > Cu(15)CeMgAlO-550 > Cu(15)CeMgAlO-650. Notably, the apparent activation energy decreases with increasing the calcination temperature (Table 5), suggesting that higher calcination temperature gives rise to more reactive catalytic sites in Cu(15)CeMgAlO system within the calcination temperature range studied. This could be attributed to a strengthened Cu-Ce interaction with increasing calcination temperature as suggested by the observed increase of both Cu(II)/Cu and Ce(IV)/Ce surface atomic ratios (Fig. S4) and by the evolution of the easiness of reduction in the H₂-TPR studies. Indeed, it has been shown that the calcination process favors the Cu-Ce interaction in the mixed oxides obtained from LDH precursors [64]. This interaction results in an easier reduction of Cu²⁺ species due to synergistic involvement of the Ce⁴⁺/Ce³⁺ redox couple according to the equilibrium:



with beneficial consequences on the catalytic ability of the mixed oxide functioning via a heterogeneous redox mechanism to oxidize methane. Notably, for the catalysts calcined at different temperatures, a linear increase of the intrinsic activity with the hydrogen consumption in H₂-TPR experiments has been observed (Fig. 10). This suggests that all the reducible species evidenced in the H₂-TPR experiments are involved in the catalytic process and confirms the redox mechanism. It is noteworthy that in the CuO-CeO₂ system the optimum of the calcination temperature, studied in the range from 500 to 900 °C, was found to be 700 °C where the most stable state of Cu-Ce-O solid solution was formed [65].

Fig. 11a shows the effect of GHSV on the catalytic activity of the Cu(15)CeMgAlO mixed oxide. It can be observed that the light-off curve slightly shifts toward higher temperatures with increasing the GHSV while keeping constant the concentration of methane in the feed gas at 1 vol. %. Thus, T_{50} increases from 462 to 466 and 469 °C when the GHSV has been increased from 16000 to 20000 and 30000 h⁻¹, respectively. A shift of the light-off curve toward higher

temperatures is also observed when the concentration of methane in the feed gas has been increased from 1 to 3 vol. %, for the reaction performed over Cu(15)CeMgAlO catalyst at a constant GHSV of 16000 h^{-1} , as shown in Fig. 11b. Indeed, T_{10} and T_{50} increase from 380 to 385 and 390 °C and from 462 to 466 and 468 °C when the concentration of methane has been increased from 1 to 2 and 3 vol. %, respectively. This behavior has already been observed for a Pd/Al₂O₃ catalyst and was attributed to methane reaction orders lower than 1 [66].

It has been previously shown that both CuMgAlO [32] and CeMgAlO [33] catalysts obtained from LDH precursors display good stabilities during the complete oxidation of methane. Nevertheless, the stability of the Cu(15)CeMgAlO catalyst, the most active one in the series studied, was checked by maintaining it on stream at 550 °C for more than 50 h. Fig. 12 shows no effect of time on stream on the catalytic activity of the Cu(15)CeMgAlO catalyst suggesting its good stability, at least for the reaction conditions and the reaction time chosen.

4. Conclusion

A series of Cu(x)CeMgAlO mixed oxides with fixed Ce content of 10 at. % with respect to cations and Mg/Al mol ratio of 3, but with different copper loadings x in the range from 6 to 18 at. % were prepared by thermal decomposition at 750 °C of precursors consisting of poorly crystallized LDH and boehmite AlOOH phases. They have slit-like bimodal mesopores and relatively high surface areas, which regularly decrease from 169 to $108 \text{ m}^2 \text{ g}^{-1}$ with increasing the Cu content, and consist of periclase-like Mg(Al)O mixed oxide and CeO₂ fluorite phases, except for Cu(18)CeMgAlO, which also contains well developed CuO crystallites. At low Cu content highly dispersed Cu-doped ceria crystallites coexist with oligomeric $(\text{Cu}^{2+} - \text{O}^{2-} - \text{Cu}^{2+})_n^{2+}$ species in the Mg(Al)O matrix, while at high Cu content larger ceria crystallites less exposed on the catalyst surface coexist with separate CuO particles enriching the surface. The Cu(II)/Cu surface atomic ratio was shown to be a key factor controlling the catalytic activity of the Cu(x)CeMgAlO catalysts. With the highest Cu(II)/Cu surface atomic ratio, the Cu(15)CeMgAlO mixed oxide is the most active catalyst in this series, with a T_{50} value of only ca. 45 °C higher than that of an industrial Pd/Al₂O₃ catalyst. Its enhanced catalytic activity is attributed to an excellent dispersion of CuO, oligomeric $(\text{Cu}^{2+} - \text{O}^{2-} - \text{Cu}^{2+})_n^{2+}$ species coexisting with tiny not XRD-visible CuO crystallites strongly interacting with ceria, which leads to a strong synergy

effect between Cu and Ce. The catalytic sites are located at the CuO-CeO₂ particles interface. Decreasing the calcination temperature of the Cu(15)CeMgAl precursor from 750 to 650 and 550 °C results in mixed oxides with higher surface areas and, hence, higher catalytic activities in terms of T₅₀, which for the Cu(15)CeMgAlO-550 system is only ca. 25 °C higher than that of the industrial Pd/Al₂O₃ catalyst. However, in terms of intrinsic reaction rates the most active catalyst is that calcined at 750 °C accounting for a strengthened Cu-Ce interaction with increasing calcination temperature. A shift of the light-off curve obtained over Cu(15)CeMgAlO catalyst toward higher temperatures with increasing the methane content in the feed gas is observed accounting for methane reaction orders lower than 1. A good stability on stream of the Cu(15)CeMgAlO catalyst calcined at 750 °C was noted.

References

1. J.J. Spivey, *Ind. Eng. Chem. Res.* 26 (1987) 2165-2180.
2. W.J. Cooper, L.A. Hollway, *Nature* 384 (1996) 313-315.
3. B.J. Finlayson-Pitts, J.N. Pitts, *Science* 276 (1997) 1045-1051.
4. A.C. Lewis, N. Carslaw, P.J. Marriott, R.M. Kinghorn, P. Morrison, A.L. Lee, M.J. Pilling, *Nature* 405 (2000) 778-781.
5. M. Lopez, O.A. Sherwood, E.J. Dlugokencky, R. Kessler, L. Giroux, D.E.J. Worthy, *Atmos. Environ.* 164 (2017) 280-288.
6. D.C. Quiros, J. Smith, A. Thiruvengadam, T. Huai, S. Hu, *Atmos. Environ.* 168 (2017) 36-45.
7. J. Kirchnerova, M. Alifanti, B. Delmon, *Appl. Catal. A* 231 (2002) 65-80.
8. Y. Moro-Oka, Y. Morikawa, A. Ozaki, *J. Catal.* 7 (1967) 23-32.
9. P.O. Thevenin, P.G. Menon, S.G. Järås, *CATTECH* 7 (2003) 10-22.
10. D. Ciuparu, M.R. Lyobovsky, E. Altman, L.D. Pfefferle, A. Datye, *Catal. Rev. Sci. Eng.* 44 (2002) 593-649.
11. C. Batiot-Dupeyrat, F. Martinez-Ortega, M. Ganne, J.M. Tatibouet, *Appl. Catal. A* 206 (2001) 205-215.
12. S. Pengpanich, V. Meeyoo, T. Rirksomboon, K. Bunyakiat, *Appl. Catal. A* 234 (2002) 221-233.

13. A.Y. Zarur, J.Y. Ying, *Nature* 403 (2000) 65-67.
14. A.C. Gluhoi, N. Bogdanchikova, B.E. Nieuwenhuys, *Catal. Today* 113 (2006) 178-181.
15. T.V. Choudhary, S. Banerjee, V.R. Choudhary, *Appl. Catal. A* 234 (2002) 1-23.
16. R.A. Dalla Betta, *Catal. Today*, 35 (1997) 129-135.
17. E.C. Moretti, *Chem. Eng. Progr.* 98 (2002) 30-40.
18. R.M. Heck, R.J. Farrauto, "Catalytic Air Pollution Control. Commercial Technology",
Publisher: Van Nostrand Reinhold, New York, USA, 1995.
19. J.J. Spivey, J.B. Butt, *Catal. Today* 11 (1992) 465-500.
20. W.B. Li, J.X. Wang, H. Gong, *Catal. Today* 148 (2009) 81-87.
21. M. Tomatis, H.-H. Xu, J. He, X.-D. Zhang, *J. Chem.* (2016) Art. ID 8324826.
22. M. Shahzad Kamal, S.A. Razzak, M.M. Hossain, *Atmos. Environ.* 140 (2016) 117-134.
23. P. Kuśtrowski, A. Rokicińska, T. Kondratowicz, *Adv. Inorg. Chem.* 72 (2018) 385-419.
24. J. Chen, H. Arandiyana, X. Gao, J. Li, *Catal. Surv. Asia* 19 (2015) 140-171.
25. Z. Ma, *Curr. Catal.* 3 (2014) 15-26.
26. X.-D. Zhang, Y. Wang, Y.-Q. Yang, D. Chen, *Acta Phys. Chim. Sin.* 31 (2015) 1633-1646.
27. Y. Liu, J. Deng, S. Xie, Z. Wang, H. Dai, *Chin. J. Catal.* 37 (2016) 1193-1205.
28. P. Mohapatra, T. Mishra, K.M. Parida, *Key Eng. Mater.* 571 (2013) 71-91.
29. J. Li, M. Hu, S. Zuo, X. Wang, *Curr. Opin. Chem. Eng.* 20 (2018) 93-98.
30. I.-C. Marcu, A. Urdă, I. Popescu, V. Hulea, *in Sustainable Nanosystems Development, Properties and Applications*, M.V. Putz, M.C. Mirica (Eds.), IGI Global, Hershey, PA, USA, 2017, Ch. 3, p. 59-121.
31. S. Tanasoi, G. Mitran, N. Tanchoux, T. Cacciaguerra, F. Fajula, I. Săndulescu, D. Tichit, I.-C. Marcu, *Appl. Catal. A* 395 (2011) 78-86.
32. S. Tanasoi, N. Tanchoux, A. Urdă, D. Tichit, I. Săndulescu, F. Fajula, I.-C. Marcu, *Appl. Catal. A* 363 (2009) 135-142.
33. A. Urdă, I. Popescu, T. Cacciaguerra, N. Tanchoux, D. Tichit, I.-C. Marcu, *Appl. Catal. A* 464-465 (2013) 20-27.
34. M. Konsolakis, *Appl. Catal. B* 198 (2016) 49-66.
35. M. Piumetti, S. Bensaid, T. Andana, N. Russo, R. Pirone, D. Fino, *Appl. Catal. B* 205 (2017) 455-468.

36. P. Bera, K. R. Priolkar, P. R. Sarode, M. S. Hegde, S. Emura, R. Kumashiro, N. P. Lalla, *Chem. Mater.* 14 (2002) 3591-3601.
37. S. Hočevar, U.O. Krašovec, B. Orel, A.S. Aricó, H. Kim, *Appl. Catal. B* 28 (2000) 113-125.
38. M. Mogensen, N.M. Sammes, G.A. Tompsett, *Solid State Ionics* 129 (2000) 63-94.
39. P. Knauth, H. L. Tuller, *Solid State Ionics* 136-137 (2000) 1215-1224.
40. C. Zerva, C.J. Philippopoulos, *Appl. Catal. B* 67 (2006) 105-112.
41. B. Yildiz, L. Sun, ECS Meeting 2017, Abstract MA2017-01 1578.
42. H. Zhang, G. Zhang, X. Bi, X. Chen, *J. Mater. Chem. A* 1 (2013) 5934-5942.
43. B. Savova, D. Filkova, D. Crişan, M. Crişan, M. Răileanu, N. Drăgan, A. Galtayries, J.C. Védrine, *Appl. Catal. A* 359 (2009) 47-54.
44. P.F. Schofield, C.M.B. Henderson, S.A.T. Redfern, G. Van der Laan, *Phys. Chem. Minerals* 20 (1993) 375-381.
45. M.C. Biesinger, L.W.M. Lau, A.R. Gerson, R.St.C. Smart, *Appl. Surf. Sci.* 257 (2010) 887-898.
46. P. Burroughs, A. Hamnett, A. F. Orchard, G. Thornton, *J. Chem. Soc. Dalton Trans.* (1976) 1686-1698.
47. E. Bêche, P. Charvin, D. Perarnau, S. Abanades, G. Flamant, *Surf. Interface Anal.* 40 (2008) 264-267.
48. X. Yu, G. Li, *J. Alloy Compd* 364 (2004) 193-198.
49. NIST X-ray Photoelectron Spectroscopy Database, NIST Standard Reference Database Number 20, National Institute of Standards and Technology, Gaithersburg MD, 20899 (2000), doi:10.18434/T4T88K
50. IUPAC, Reporting physisorption data for gas/solid system, *Pure Appl. Chem.* 57 (1985) 603-619.
51. J. Beckers, G. Rothenberg, *Dalton Trans.* (2008) 6573-6578.
52. F. Giordano, A. Trovarelli, C. de Leitenburg, M. Giona, *J. Catal.* 193 (2000) 193-273.
53. S. Basag, K. Kocoł, Z. Piwowarska, M. Rutkowska, R. Baran, L. Chmielarz, *Reac. Kinet. Mech. Catal.* 121 (2017) 225-240.
54. Y. Li, Q. Fu, M. Flytzani-Stephanopoulos, *Appl. Catal. B* 27 (2000) 179-191.
55. L. Kundakovic, M. Flytzani-Stephanopoulos, *Appl. Catal. A* 171 (1998) 13-29.

56. M. Răciulete, G. Layrac, F. Papa, C. Negrilă, D. Tichit, I.-C. Marcu, *Catal. Today* 306 (2018) 276-286.
57. Lever, A.B.P. *Inorganic electronic spectroscopy*, 2nd ed.; Elsevier, Amsterdam, London, New York, 1984; pp. 553-572, ISBN 0444416994.
58. M. Răciulete, G. Layrac, D. Tichit, I.-C. Marcu, *Appl. Catal. A* 477 (2014) 195-204.
59. Y.F. Lu, F.C. Chou, F.C. Lee, C.Y. Lin, D.H. Tsai, *J. Phys. Chem. C* 120 (2016) 27389-27398.
60. B. Kucharczyk, *Polish J. Chem. Technol.* 13 (2011) 57-62.
61. I. Popescu, N. Tanchoux, D. Tichit, I.-C. Marcu, *Appl. Catal. A* 538 (2017) 81-90.
62. Z. Jiang, Z. Hao, J. Yu, H. Hou, C. Hu, J. Su, *Catal. Lett.* 99 (2005) 157-163.
63. Z.G. Liu, S.H. Chai, A. Binder, Y.Y. Li, L.T. Ji, S. Dai, *Appl. Catal. A* 451 (2013) 282-288.
64. Z. Chang, N. Zhao, J. Liu, F. Li, D.G. Evans, X. Duan, C. Forano, M. de Roy, *J. Solid State Chem.* 184 (2011) 3232-3239.
65. C.R. Jung, J. Han, S.W. Nam, T.-H. Lim, S.-A. Hong, H.-I. Lee, *Catal. Today* 93-95 (2004) 183-190.
66. Z. Yang, P. Yang, L. Zhang, M. Guoa, Y. Yan, *RSC Adv.* 4 (2014) 59418-59426.

FIGURES CAPTION

Figure 1. XRD patterns of the Cu(x)CeMgAlO precursors as prepared. Symbols: # - LDH phase; * - boehmite (AlOOH) phase.

Figure 2. XRD patterns of the Cu(x)CeMgAlO mixed oxides calcined at 750 °C (a) and of the Cu(15)CeMgAlO mixed oxides calcined at different temperatures (b). Symbols: x - CuO tenorite phase; ◆ - CeO₂ fluorite phase; ▼ - Mg(Al)O mixed oxide periclase-like phase.

Figure 3. O 1s core level (a) and C 1s core level (b) XPS spectra of the Cu(x)CeMgAlO mixed oxide catalysts: CeMgAlO (a), Cu(6)CeMgAlO (b), Cu(9)CeMgAlO (c), Cu(12)CeMgAlO (d), Cu(15)CeMgAlO (e), Cu(15)CeMgAlO-650 (f), Cu(15)CeMgAlO-550 (g), Cu(18)CeMgAlO (h).

Figure 4. Cu 2p core level (a) and Ce 3d core levels (b) XPS spectra of the Cu(x)CeMgAlO mixed oxide catalysts: Cu(6)CeMgAlO (a), Cu(9)CeMgAlO (b), Cu(12)CeMgAlO (c), Cu(15)CeMgAlO (d), Cu(15)CeMgAlO-650 (e), Cu(15)CeMgAlO-550 (f), Cu(18)CeMgAlO (g), CeMgAlO (h).

Figure 5. H₂-TPR profiles of the Cu(x)CeMgAlO mixed oxides calcined at 750 °C (a) and of the Cu(15)CeMgAlO mixed oxides calcined at different temperatures (b).

Figure 6. Amount of Ce⁴⁺ species reduced in H₂-TPR experiments vs. ceria particle size in the Cu(x)CeMgAlO mixed oxides calcined at 750 °C.

Figure 7. DR-UV-Vis spectra of the Cu(x)CeMgAlO mixed oxides: Cu(6)CeMgAlO (a), Cu(9)CeMgAlO (b), Cu(12)CeMgAlO (c), Cu(15)CeMgAlO (d), Cu(15)CeMgAlO-650 (e), Cu(15)CeMgAlO-550 (f), Cu(18)CeMgAlO (g).

Figure 8. The light-off curves for the combustion of methane over Cu(x)CeMgAlO catalysts calcined at 750 °C (a) and over Cu(15)CeMgAlO catalysts calcined at different temperatures (b) compared with that of an industrial reference Pd/Al₂O₃ catalyst. Reaction conditions: 1 vol. % methane in air, GHSV of 16000 h⁻¹, 1 cm³ of catalyst.

Figure 9. Variation of the Cu(II)/Cu surface atomic ratio and the intrinsic methane conversion rate at 380 and 400 °C as a function of the Cu content in the Cu(x)CeMgAlO mixed oxide catalysts.

Figure 10. Intrinsic activities measured at 380 °C vs. hydrogen consumption in the H₂-TPR experiments for the Cu(15)CeMgAlO catalysts calcined at different temperatures.

Figure 11. Effects of gas hourly space velocity at constant concentration of methane in the feed gas of 1 vol. % (a) and of methane concentration in the feed gas at constant GHSV of 16000 h⁻¹ (b) on methane conversion over Cu(15)CeMgAlO catalyst.

Figure 12. Conversion of methane versus time on stream for the reaction at 550 °C over Cu(15)CeMgAlO catalyst. Reaction conditions: 1 vol. % CH₄ in air and GHSV of 16000 h⁻¹, 1 cm³ of catalyst.

Table 1. Textural properties and crystallographic data of Cu(x)CeMgAlO catalysts.

Catalyst	Surface area (m ² g ⁻¹)	Pore volume (cm ³ g ⁻¹)	Pore size ^a (nm)	CeO ₂ lattice parameter (nm)	CeO ₂ crystallite size (nm)
Ce(10)MgAlO	52	n.d. ^b	n.d. ^b	0.5375	15.2
Cu(6)CeMgAlO	169	0.239	3.9 and 7.4	0.5403	6.3
Cu(9)CeMgAlO	148	0.236	3.9 and 9.0	0.5408	7.9
Cu(12)CeMgAlO	121	0.237	3.7 and 11.5	0.5412	9.6
Cu(15)CeMgAlO	120	0.225	3.7 and 11.4	0.5415	12.2
Cu(18)CeMgAlO	108	0.194	3.7 and 10.1	0.5418	15.1
Cu(15)CeMgAlO- 650	144	0.299	3.7 and 9.0 ^c	0.5415	4.1
Cu(15)CeMgAlO- 550	156	0.305	4.1 and 9.0 ^c	0.5399	3.1

^a Maxima of pore size distribution. ^b Not determined. ^c Shoulder.

Table 2. Chemical composition of the LDH precursors and calcined oxide catalysts determined by EDX spectroscopy.

Precursors	Atomic content (%)				Atomic ratio		Oxides	Atomic content (%)				Atomic ratio	
	Cu	Ce	Mg	Al	Mg/Al	Cu/Ce		Cu	Ce	Mg	Al	Mg/Al	Cu/Ce
							CeMgAlO	0	11.0	66.5	22.5	3.0	0
Cu(6)CeMgAl	6.8	10.3	62.2	20.6	3.0	0.7	Cu(6)CeMgAlO	6.9	9.8	62.7	20.6	3.0	0.7
Cu(9)CeMgAl	11.6	11.3	58.4	18.7	3.1	1.0	Cu(9)CeMgAlO	11.8	11.2	57.2	19.7	2.9	1.0
Cu(12)CeMgAl	15.3	12.9	53.3	18.6	2.9	1.2	Cu(12)CeMgAlO	13.8	11.6	56.4	18.2	3.1	1.2
Cu(15)CeMgAl	20.4	11.9	50.5	17.2	2.9	1.7	Cu(15)CeMgAlO	17.2	10.8	54.0	18.1	3.0	1.6
Cu(18)CeMgAl	20.0	10.0	52.1	17.9	2.9	2.0	Cu(18)CeMgAlO	20.0	9.1	52.8	18.1	2.9	2.2

Table 3. XPS analysis of the mixed oxide catalysts.

Sample	Cu	Ce	Mg	Al	O	C	Surface atomic ratios					
	(at. %)	(at. %)	(at. %)	(at. %)	(at. %)	(at. %)	Cu/(Cu+Ce+Mg+Al) %	Ce/(Cu+Ce+Mg+Al) %	Cu/Ce	Mg/Al	Cu(II)/Cu	Ce(IV)/Ce
CeMgAlO	-	0.9	13.1	5.9	49.9	30.2	-	4.5	-	2.2	-	0.80
Cu(6)CeMgAlO	2.0	1.5	18.4	6.5	60.2	11.3	7.1	5.3	1.3	2.8	0.77	0.94
Cu(9)CeMgAlO	4.4	2.8	18.6	8.0	60.7	5.5	13.0	8.3	1.6	2.3	0.80	0.95
Cu(12)CeMgAlO	5.6	2.5	17.9	7.0	52.7	14.2	17.0	7.6	2.2	2.6	0.79	0.94
Cu(15)CeMgAlO	6.8	1.8	17.6	8.2	58.3	7.5	19.8	5.2	3.8	2.2	0.90	0.93
Cu(18)CeMgAlO	6.2	1.5	17.7	8.1	54.3	12.2	18.5	4.5	4.1	2.2	0.86	0.83
Cu(15)CeMgAlO-650	6.9	1.9	16.0	7.3	61.0	6.9	21.5	5.9	3.6	2.2	0.81	0.89
Cu(15)CeMgAlO-550	5.7	2.1	16.0	7.4	57.4	11.4	18.3	6.7	2.7	2.2	0.78	0.86

^a Reference binding energy: C1s = 284.8 eV.

Table 4. Hydrogen consumptions in the H₂-TPR experiments.

Catalyst	Total H ₂ consumption (mmol g ⁻¹)	H ₂ consumption (mmol g ⁻¹) for		Amount of Ce ⁴⁺ species reduced (%)
		Cu reduction ^a	Ce reduction ^b	
CeMgAlO	0.188	-	0.188	26.7
Cu(6)CeMgAlO	1.761	1.191	0.570	67.4
Cu(9)CeMgAlO	2.207	1.916	0.291	31.9
Cu(12)CeMgAlO	2.345	2.199	0.146	15.9
Cu(15)CeMgAlO	2.844	2.727	0.117	13.7
Cu(18)CeMgAlO	3.256	3.231	0.025	3.5
Cu(15)CeMgAlO- 650	2.580	2.580 ^c	0	0
Cu(15)CeMgAlO- 550	2.727	2.727	0	0

^a Assuming the total reduction of all Cu²⁺ species.

^b Assuming the reduction Ce⁴⁺ → Ce³⁺.

^c Only 94.6 % of Cu²⁺ species are reduced.

Table 5. Catalytic performances in methane total oxidation of the catalysts studied.^a

Catalyst	T ₁₀ (°C)	T ₅₀ (°C)	T ₉₀ (°C)	Reaction rate at 380 °C		E _a (kJ mol ⁻¹)
				Specific (10 ⁷ mol g ⁻¹ s ⁻¹)	Intrinsic (10 ⁹ mol m ⁻² s ⁻¹)	
CeMgAlO	450	561	637	-	-	72.0
Cu(6)CeMgAlO	405	507	604	1.36	0.80	62.5
Cu(9)CeMgAlO	411	506	595	1.23	0.83	65.4
Cu(12)CeMgAlO	424	505	586	1.03	0.85	70.1
Cu(15)CeMgAlO	380	463	540	2.06	1.71	76.4
Cu(18)CeMgAlO	407	480	543	1.18	1.09	81.1
Cu(15)CeMgAlO- 650	383	456	535	1.87	1.30	92.2
Cu(15)CeMgAlO- 550	376	442	520	2.32	1.49	109.4

^a Reaction conditions: 1 vol. % methane in air, GHSV of 16000 h⁻¹, 1 cm³ of catalyst.

Figure

AL-AANI et al.

Figure 1.

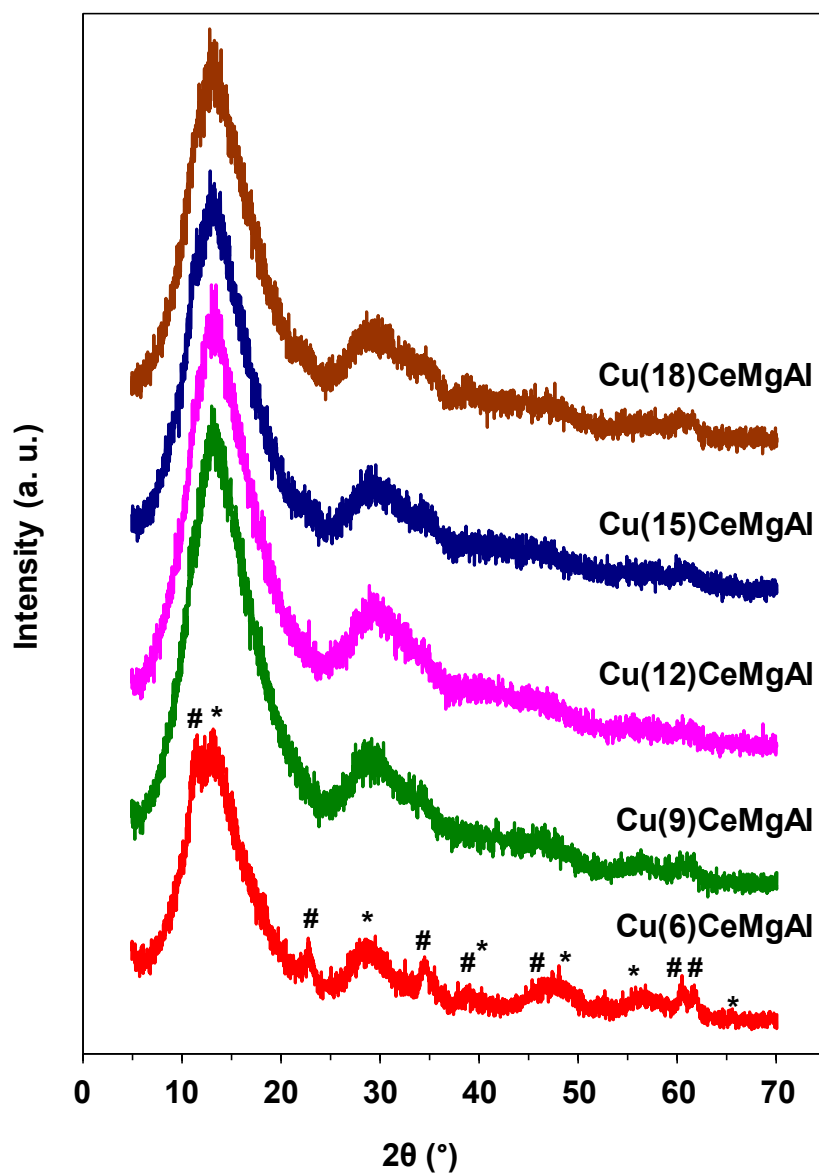
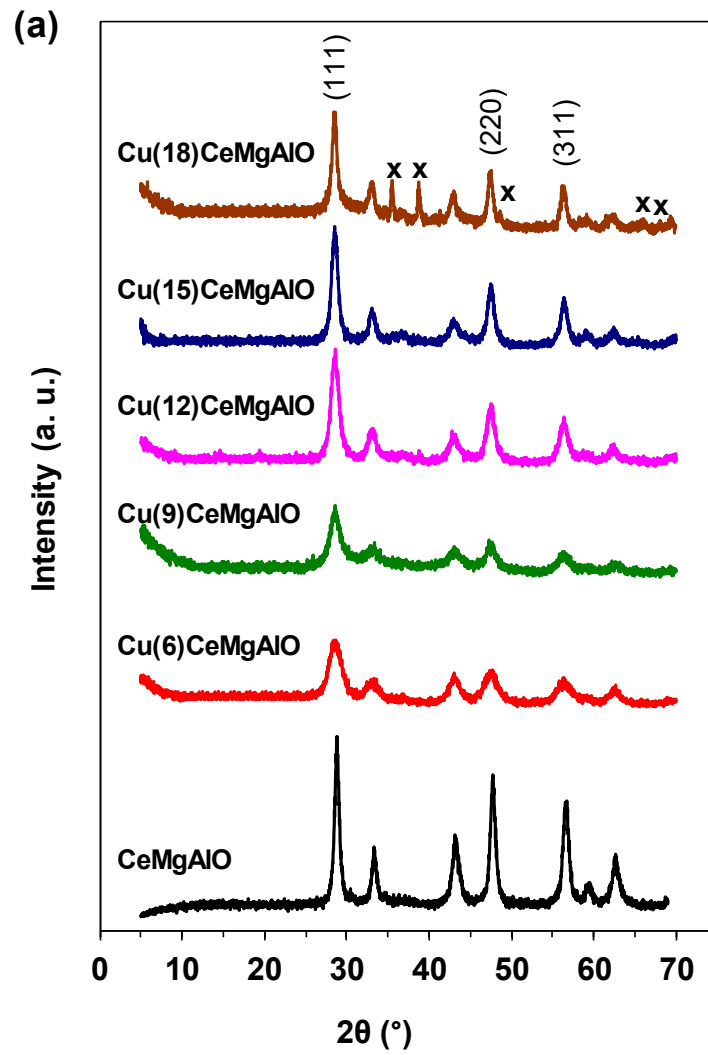


Figure 2.



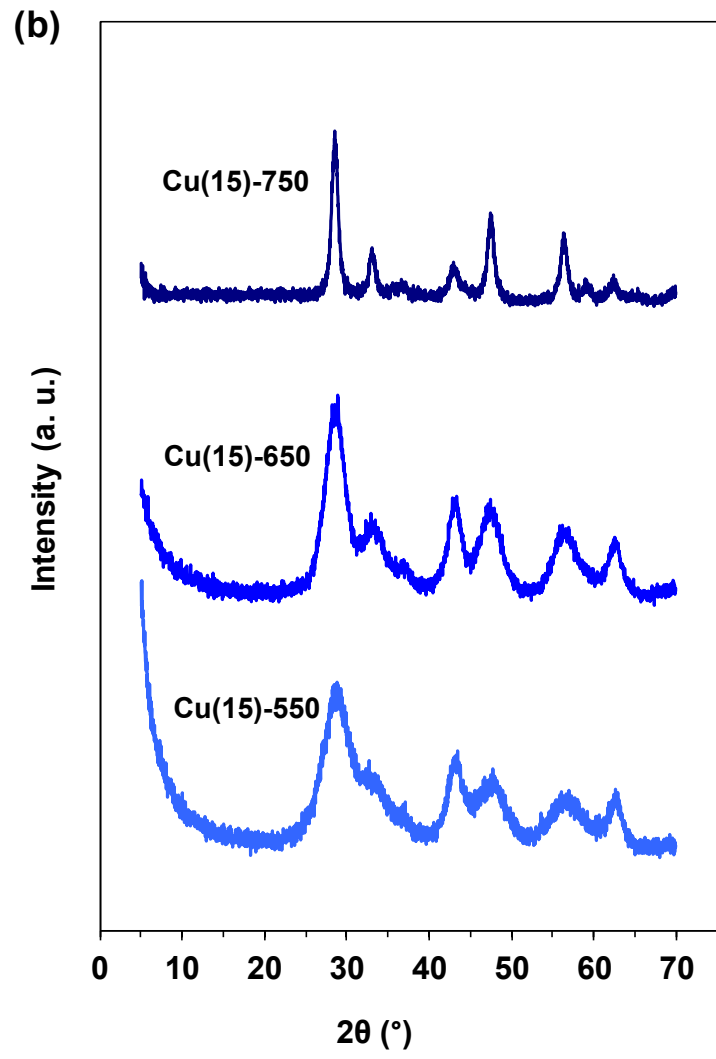
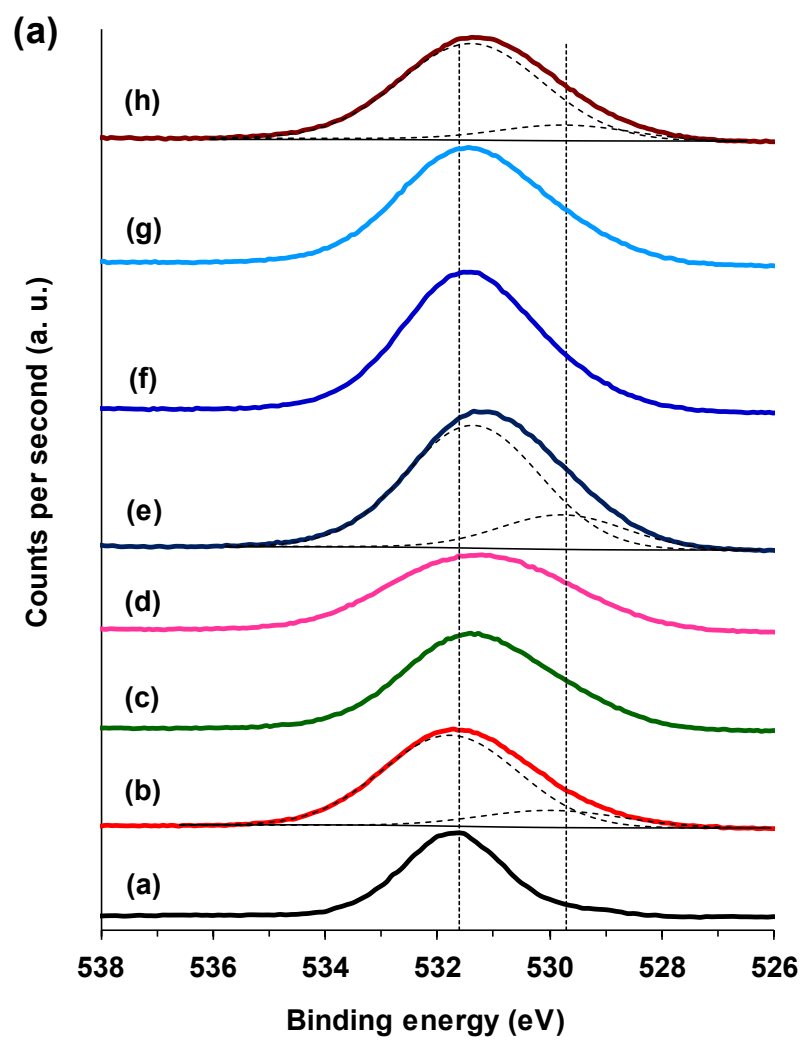


Figure 3.



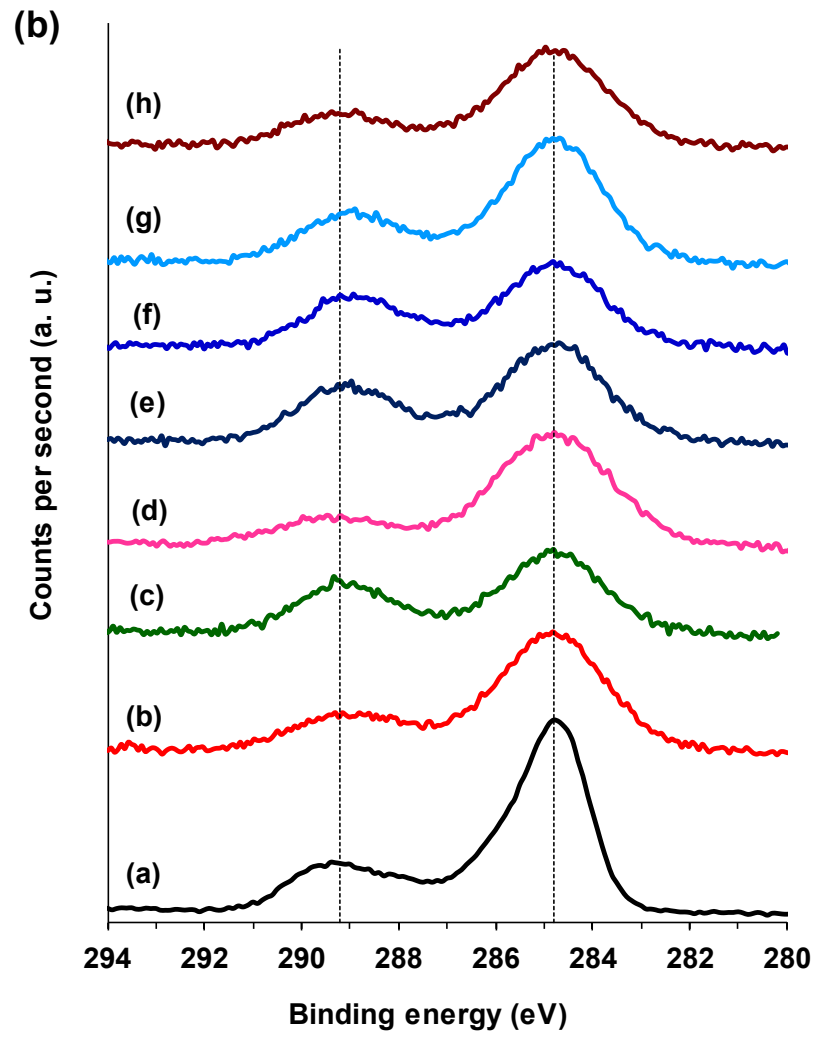
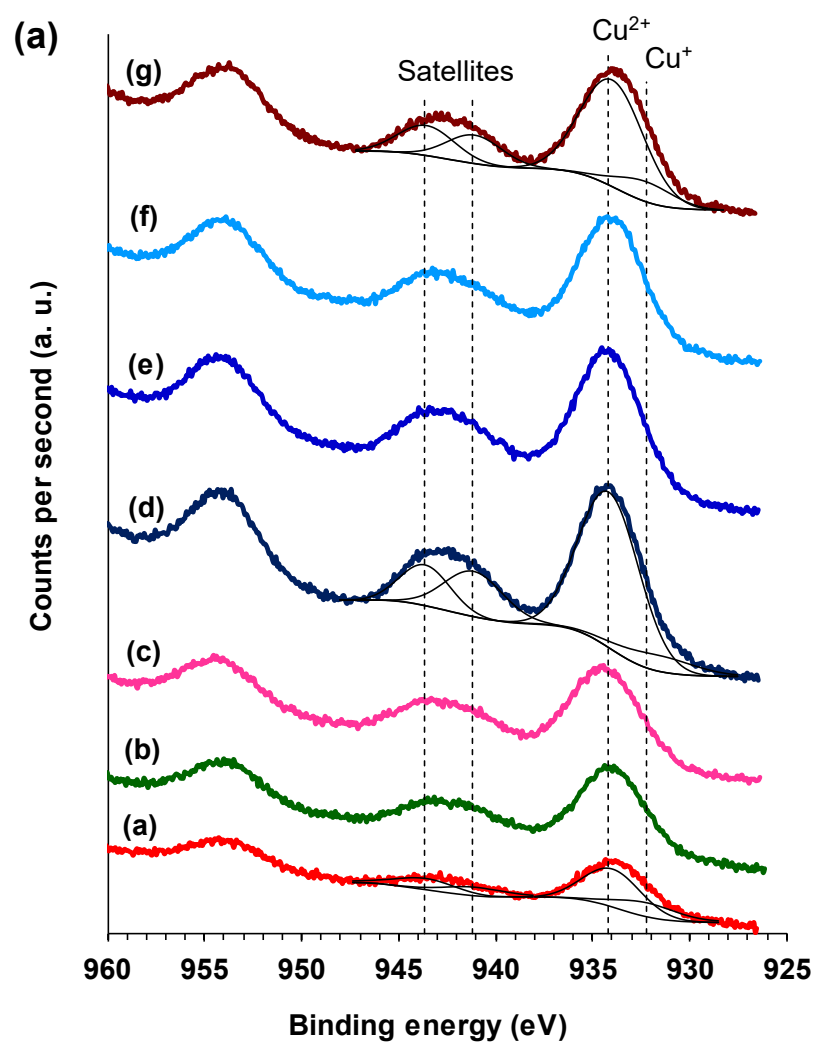


Figure 4.



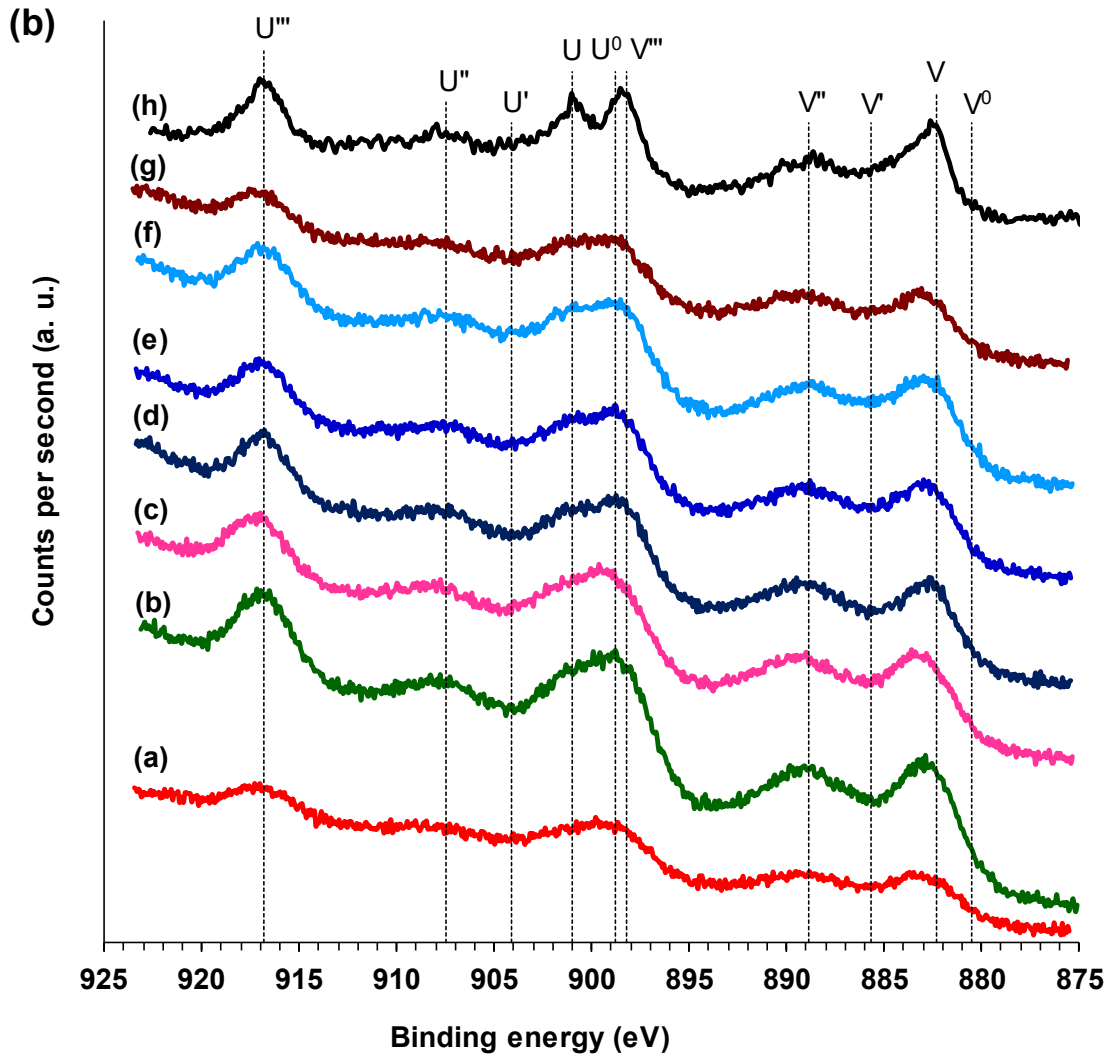
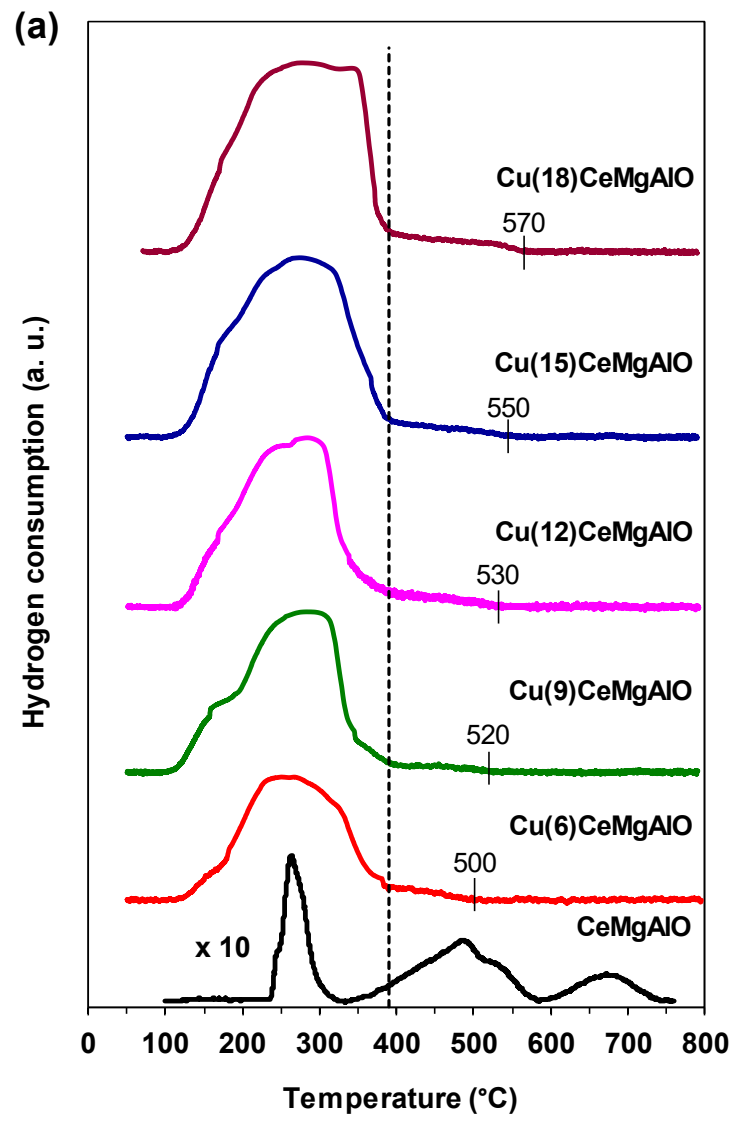


Figure 5.



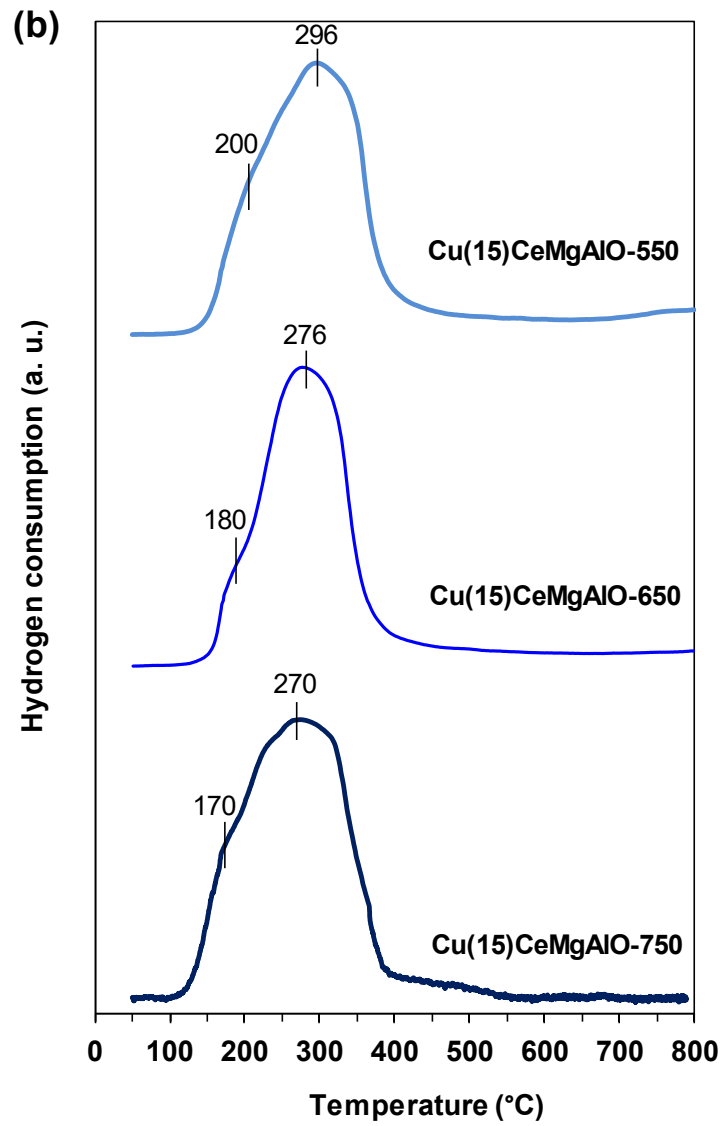


Figure 6.

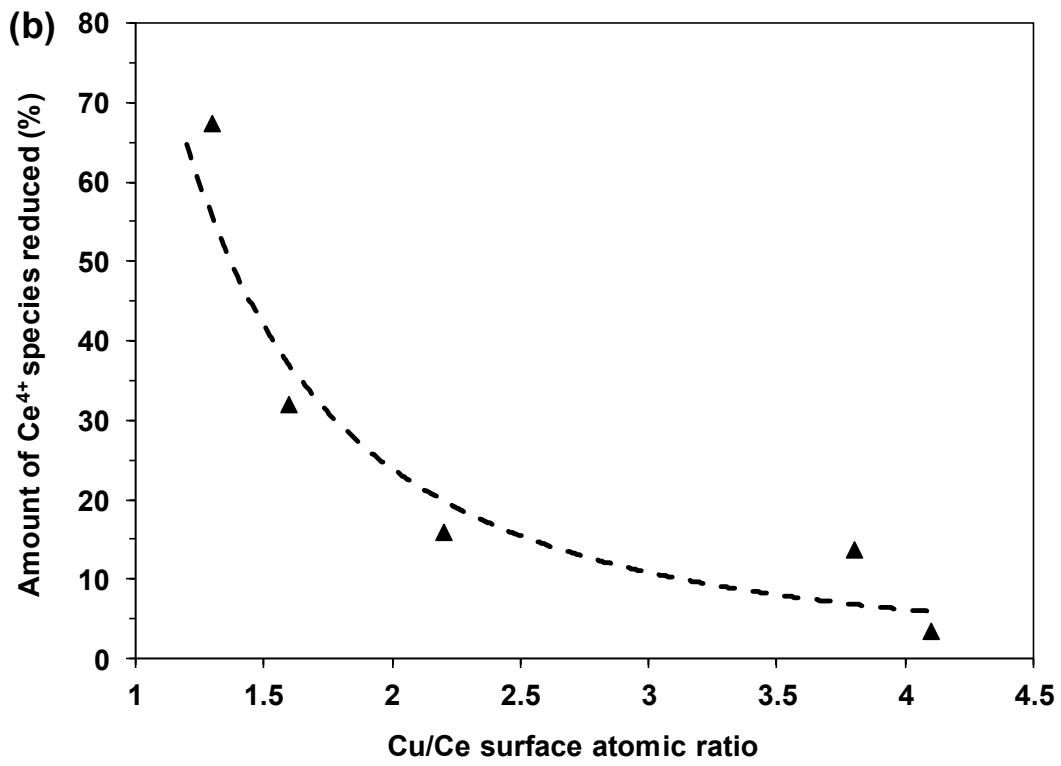
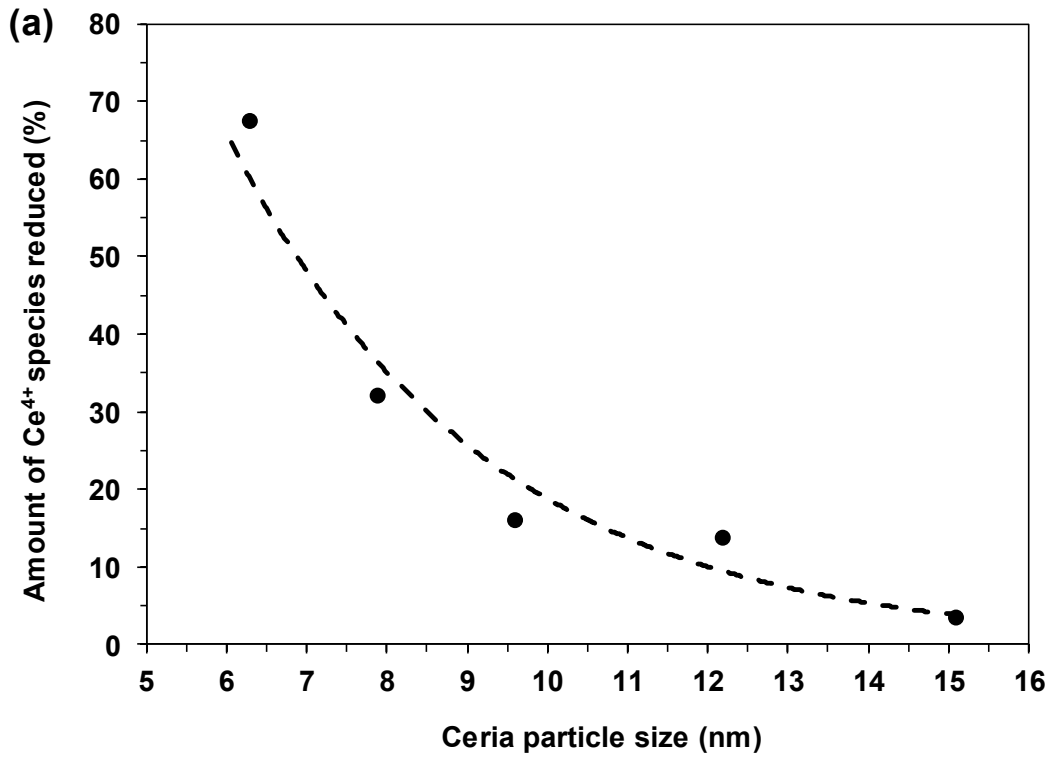


Figure 7.

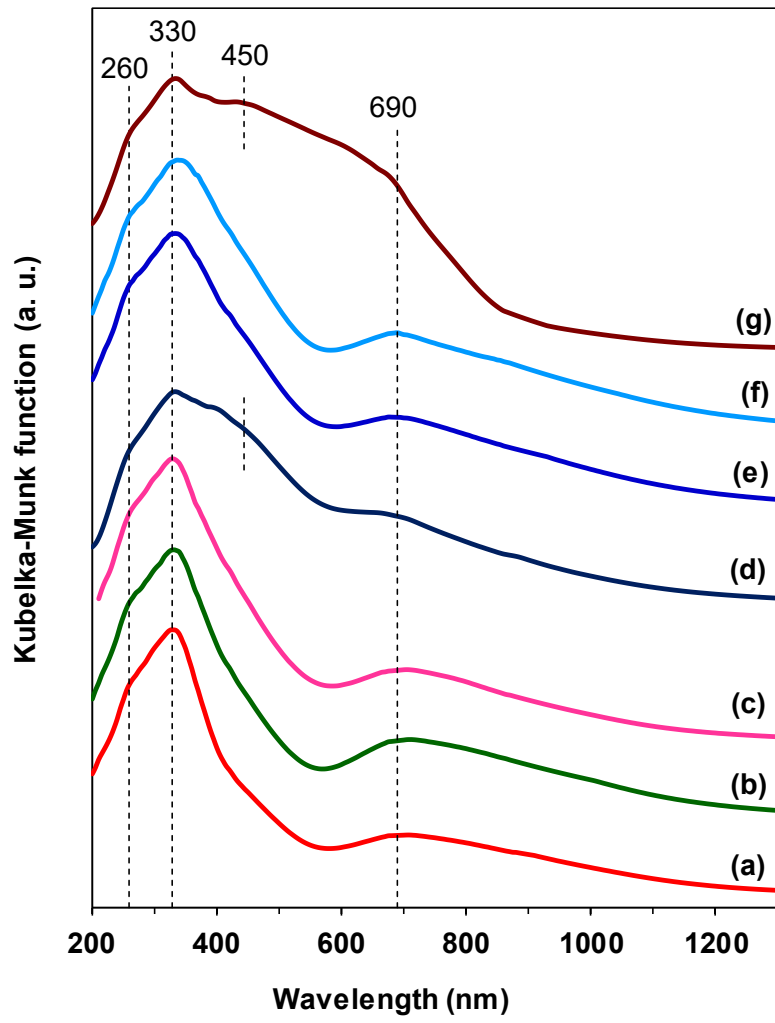
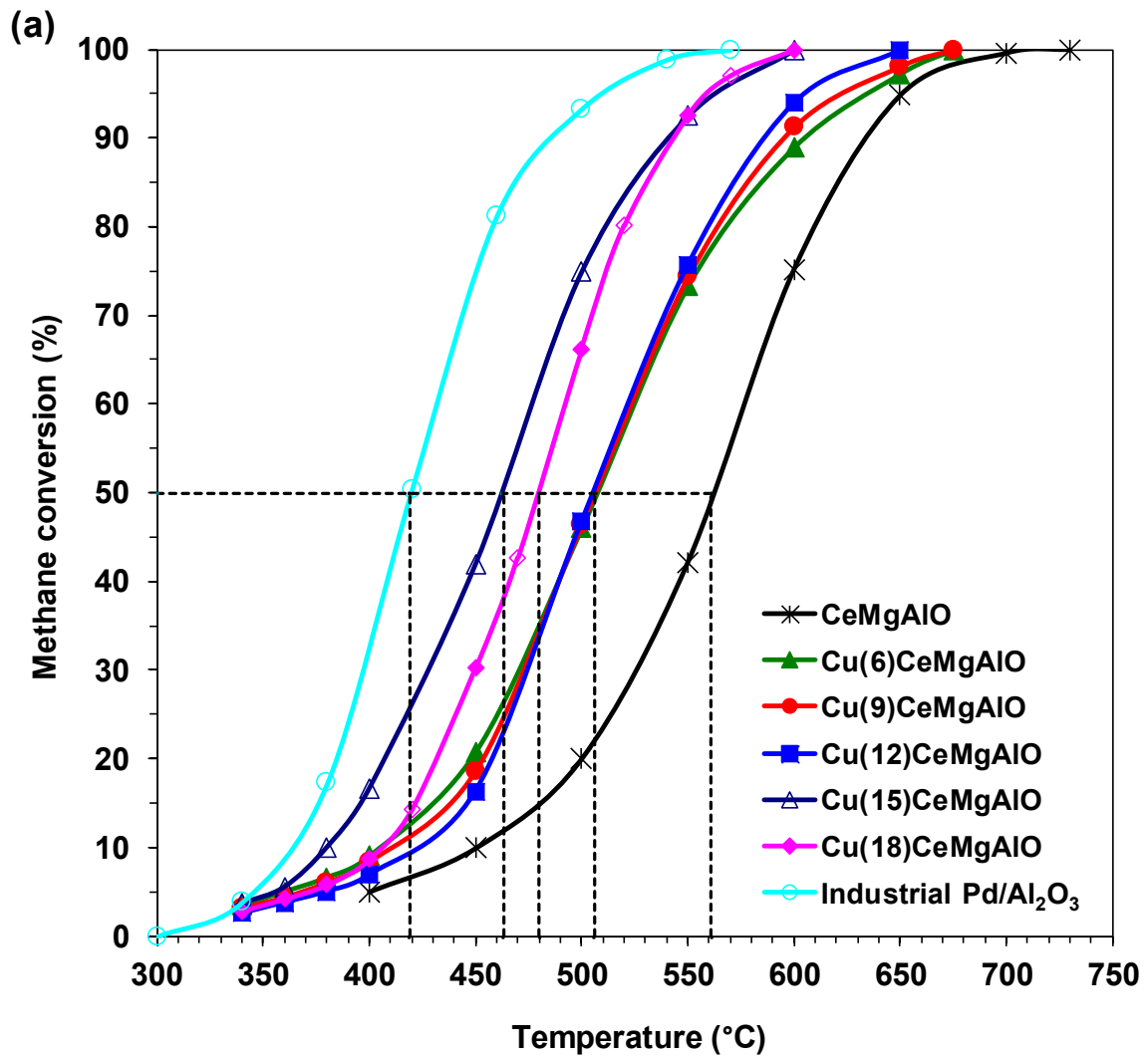


Figure 8.



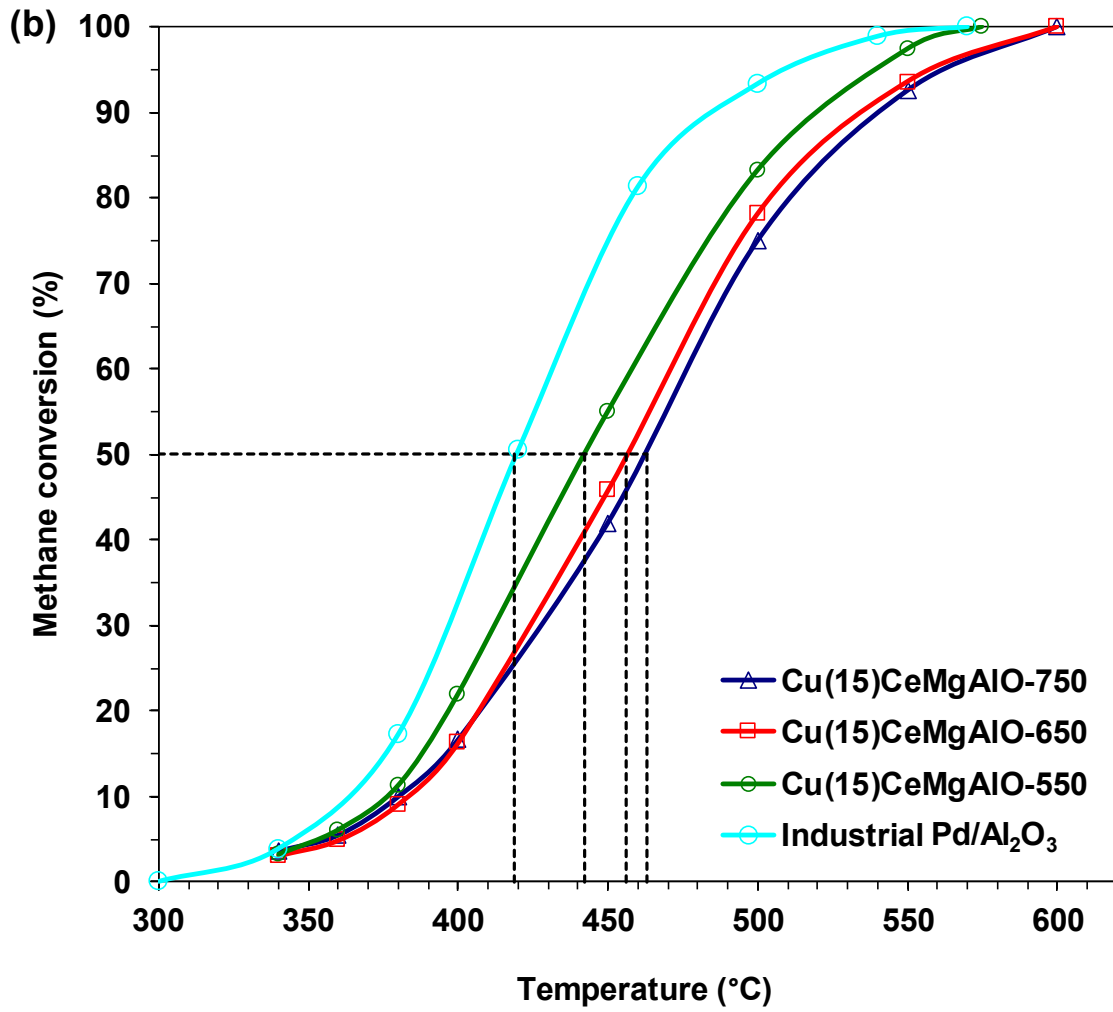


Figure 9.

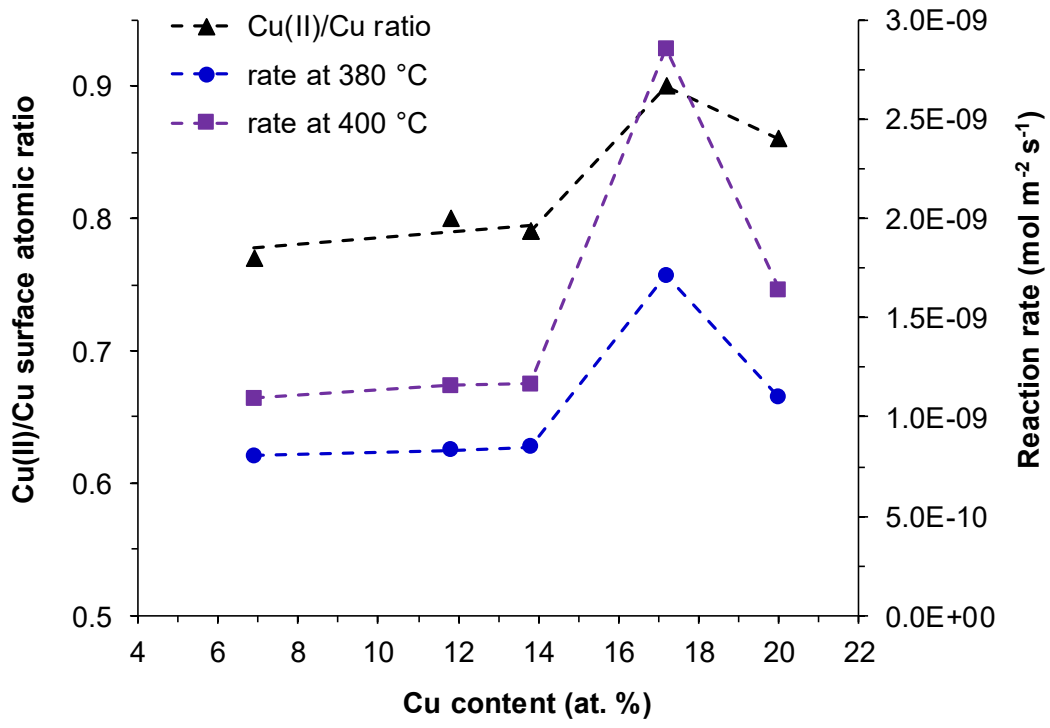


Figure 10.

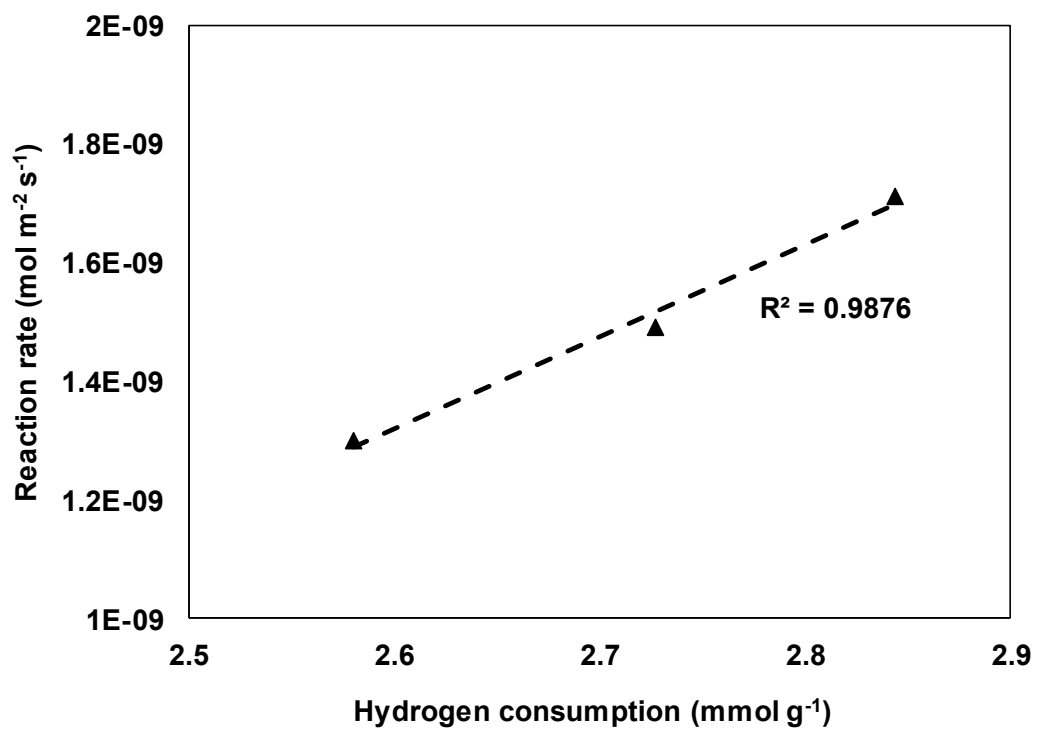
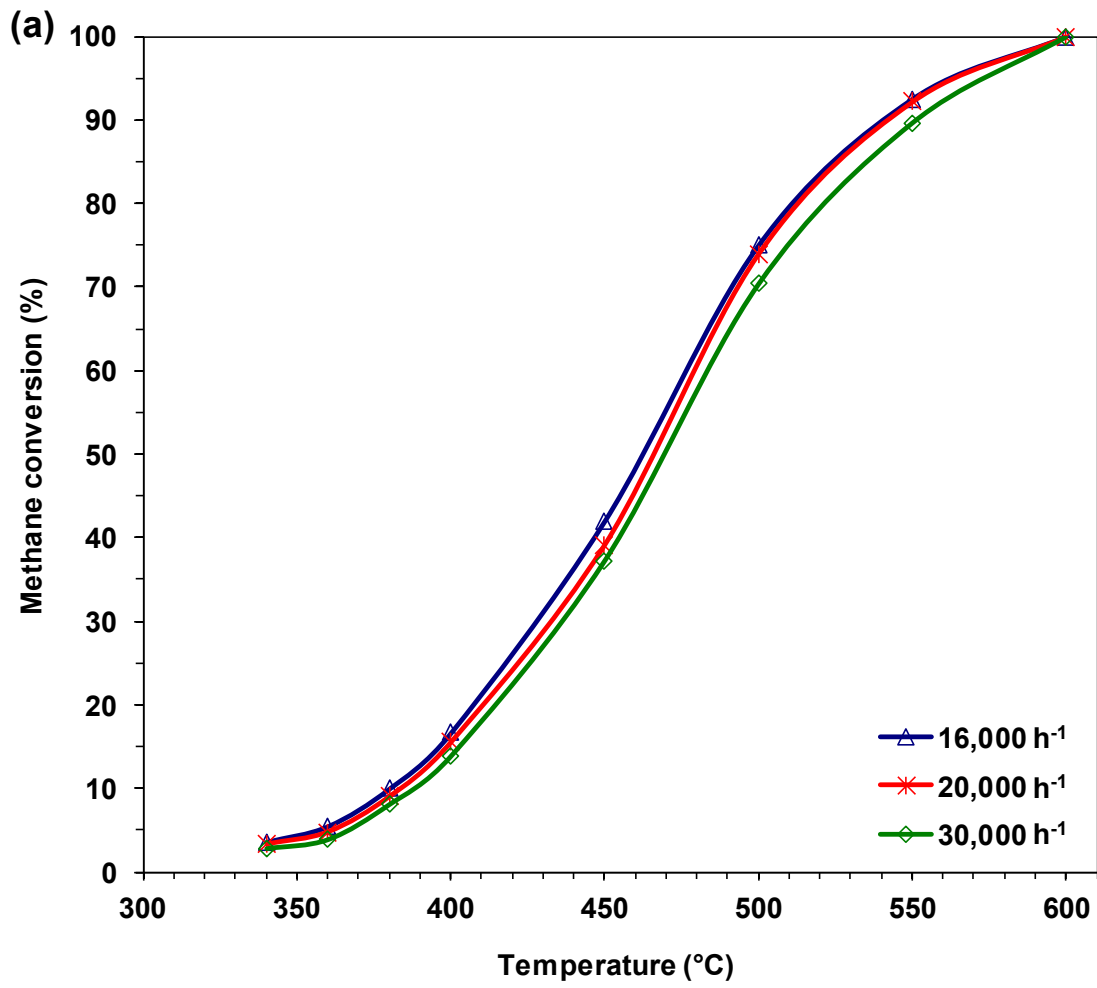


Figure 11.



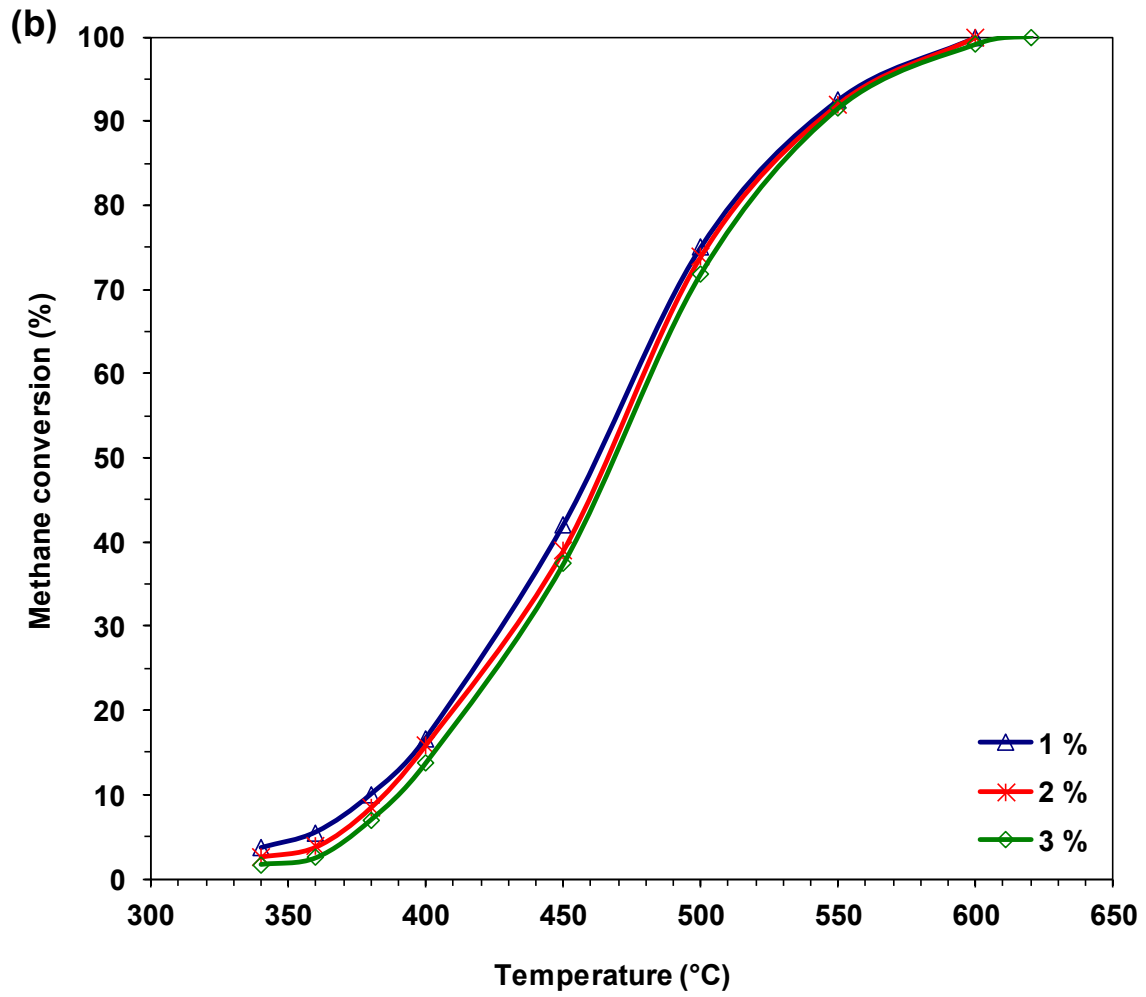
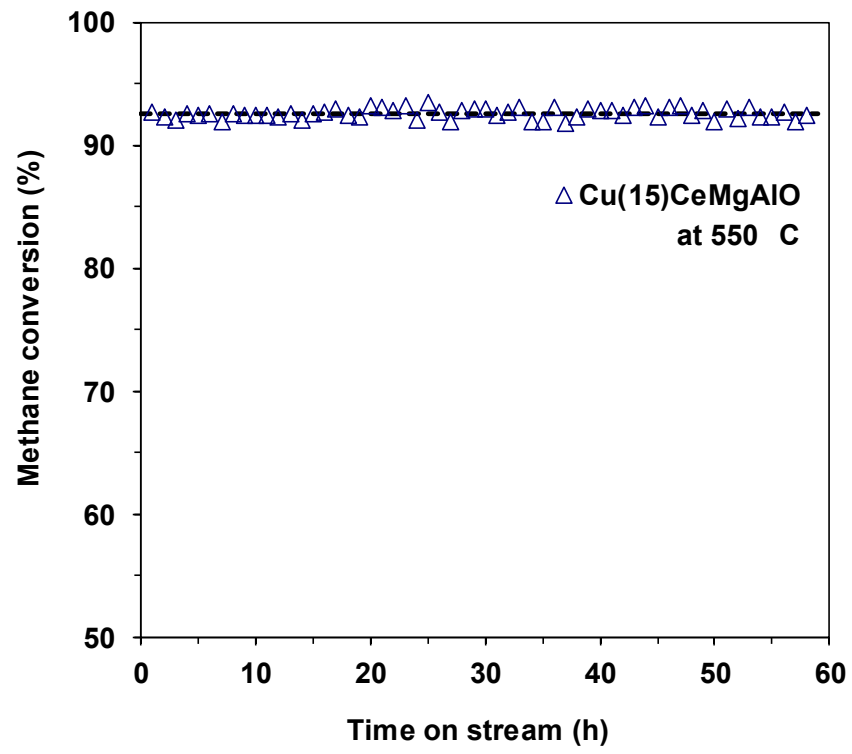


Figure 12.



Supplementary Material

[Click here to download Supplementary Material: Supplementary data.pdf](#)